"Regard man as a mine rich in gems of inestimable value. Education can, alone, cause it to reveal its treasures, and enable mankind to benefit therefrom"
Bahá'u'lláh

Chapter 2. Background

Abstract: The digital imaging revolution has provided incredible advancements in biomedical research and health care. Within pulmonary research, imaging has provided a surge of new insights into the structure and function of the lung, otherwise not apparent through whole lung mechanics.
In this chapter, an overview of the essential concepts needed for a complete understanding of the conducted research is provided. These background concepts include the structure and function of the lung, the development of histology and pathology as a gold standard for pulmonary disease research, the progression of X-ray imaging into micro-Computed Tomography, the creation of novel microscopy imaging techniques developed from laser scanning confocal microscopy, and finally the study and understanding of human disease through mouse models.

2.1 Lung Structure and Function

2.1.1 Introduction

The primary role of the lung is rapid respiration of oxygen into and carbon dioxide out of the bloodstream. The lung is also responsible for metabolizing some compounds, filtering foreign particles, removing unwanted materials from circulation, and acting as a blood reservoir. Although the lung may initially be seen as a simple organ, it is quite complex and requires well-coordinated interaction between the central nervous system, diaphragm, chest wall intercostals muscles and the circulatory system.

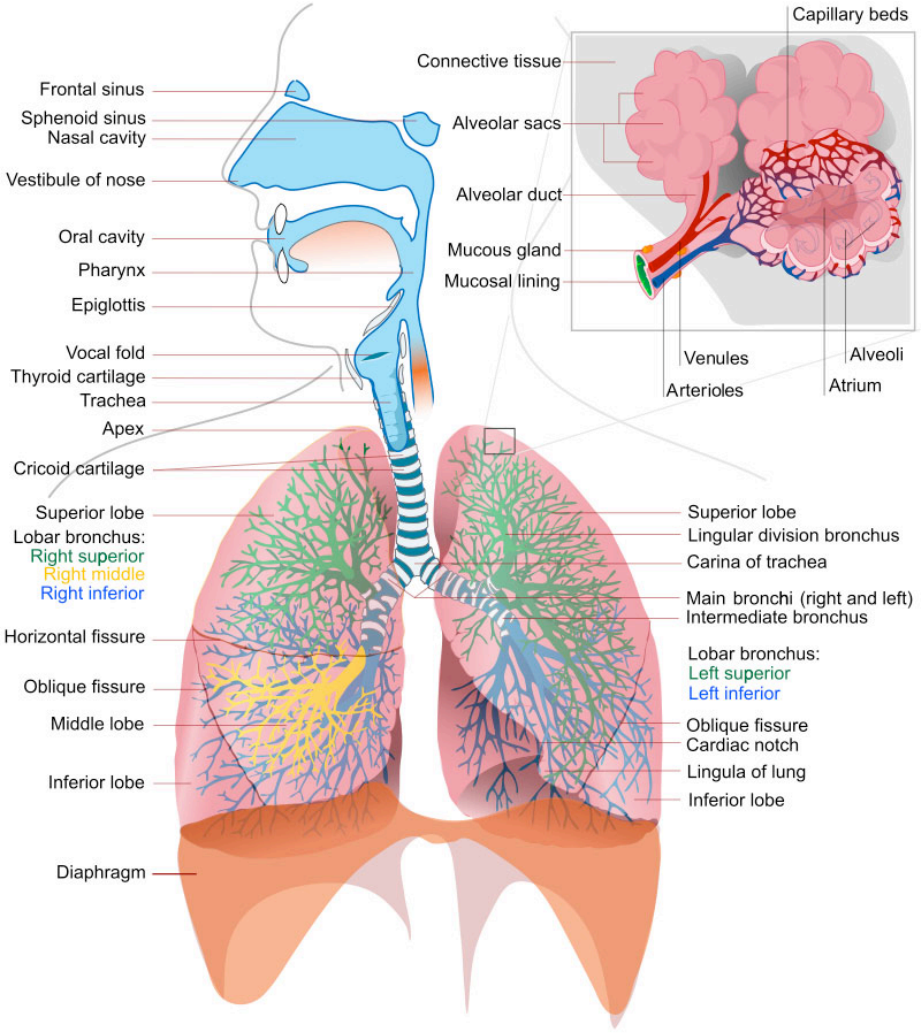

Figure 2.1: The human respiratory system, [8].

An illustration of the respiratory system is shown in Figure 2.1, here we can appreciate the complex organization of the airway structure.

2.1.2 Ventilation

The exchange of oxygen and carbon dioxide between the air and blood occurs through simple diffusion from an area of high to low partial pressure [9]. This is achieved through millions of small gas exchange units called alveoli. Alveoli are small air sacs covered with a dense capillary network with only a single cell layer separating inhaled air and the circulating bloodstream. This unique structure allows for extremely efficient gas exchange. At rest in the human, gas exchange takes 0.25 seconds or a third of the transit time of a red blood cell, thereby allowing great

leverage for increasing gas exchange at higher circulation such as in cardiovascular exercise. This capacity for gas exchange is, in part, due to the large surface presented by the alveoli. If alveoli were assumed to be spheres their total surface area would amount to approximately 85 square meters; roughly the size of a tennis court!

The lung is made up of approximately 10% solid tissue, 10% blood and 80% air [10]. The lung structure can be functionally divided into two components, the airways for ventilation and the circulatory system for perfusion. The airways can be further divided into two regions, the conducting and the respiratory region.

The conducting airways consist of a series of branching tubes that become smaller and shorter and increase in number as they fill the lung. They begin at the trachea followed by the left and right main bronchus (1^{st} generation), which then divides into lobar (2^{nd} generation) and segmental (3^{rd} generation) bronchi. They continue to divide and become smaller until they reach the terminal bronchioles (16^{th} generation); these are the smallest airways that do not contain alveoli [9]. Although the diameter of each airway decreases with each division, the total cross-sectional diameter across the lung increases dramatically, so the peripheral airway resistance decreases as depicted in Figure 2.3. The airways up to this point make up the conducting region and are responsible for providing the subsequent respiratory zone with fresh air. They do not take part in gas exchange and are often referred to as the dead air space.

The terminal bronchioles further divide into respiratory bronchioles for 2-4 generations. Here, the walls are lined with cuboidal epithelium and some muscle, indicating their primary function as conducting tubes. There are some budding alveoli found in the respiratory bronchioles, probably accounting for some gas exchange [9]. The respiratory bronchioles finally divide into alveolar ducts for 3 generations that are completely lined with alveoli and are covered in squamous epithelium with no muscle. Alveolar sacs terminate the alveolar ducts and equate to the 23^{rd} generation [11]. A diagrammatic representation of the cascading airway structure with labeled generation numbers is shown in Figure 2.2.

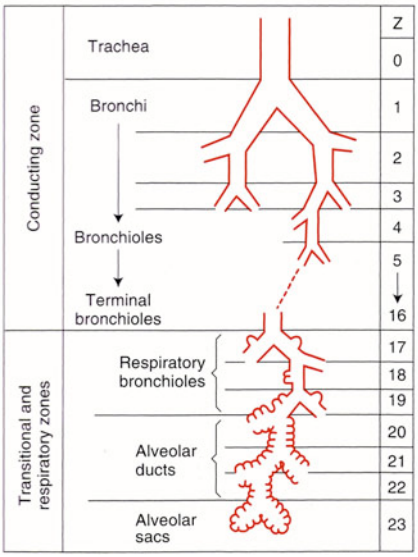

Figure 2.2: Cascading airway structure, Adapted from [9, 11].

The region comprising the respiratory bronchiole to alveoli forms the anatomical unit referred to as the acinus. In humans the nominal distance between the terminal bronchiole to the terminal alveoli is only a few mm, but this respiratory zone makes up the majority of the lung carrying 70-80% of its volume. When air is inspired into the lung it travels down the conducting airways by bulk flow and reduces in speed as the total cross-sectional area increases. Once at the respiratory region the forward velocity of the air is practically zero and diffusion becomes the primary mechanism for ventilation [9].

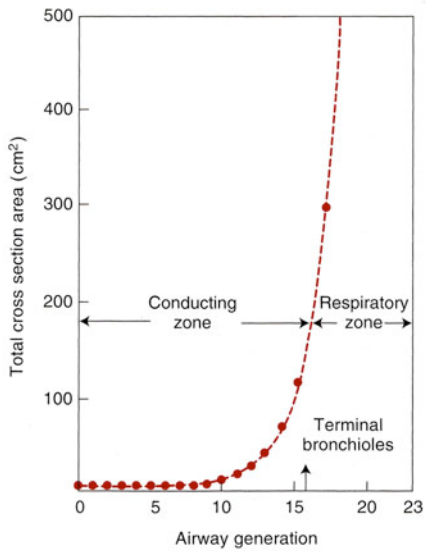

Figure 2.3: Cross sectional area vs. airway generation number, [9].

In the human lung, it has been estimated that there exists between 140-450 million alveoli, each having a mean diameter of 200-300μm [11]. Figure 2.4 represents a computer-generated depiction of the intricate terminal alveolar and capillary network. The true three-dimensional structure of the alveoli and surrounding structure in a living and breathing lung is still unknown. The alveoli are inherently unstable because of the surface tension at the liquid tissue interface. To counteract the relatively large forces that tend to collapse the alveoli, surfactant is secreted by alveolar type II cells, which line the alveoli. Surfactant has extremely low surface tension properties that significantly reduce the surface tension at the liquid tissue interface and in turn stabilize the alveoli [12-15].

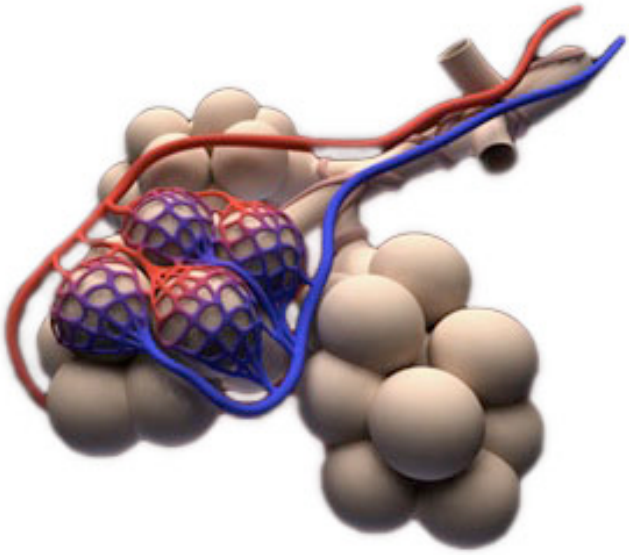

Figure 2.4: Alveolar structure, with permission from [16].

The pores of Kohn (not depicted in Figure 2.4) were first described by Adriani in 1847 [17] according to Miller [18] as small openings that connect adjacent alveoli together, and although initially considered as abnormal, they have now been identified in both normal and pathologic lungs. In the mouse, each alveolus has been reported to have 10-20 pores with diameters ranging between 1-5 microns. Recently it has also been shown that these pores are normally covered with surfactant. The function of the pores of Kohn have been controversially discussed over the past century, with the consensus, at this stage, being that they are not utilized for collateral ventilation but are limited to propagation of bacteria and cells through the lung [19-26].

2.1.3 Perfusion

The lung has two blood supply systems, the pulmonary supply, which delivers deoxygenated blood from the right side of the heart and returns oxygenated blood to the left side, and the bronchial supply, which delivers oxygenated blood to the lung tissue mainly along the large conducting airways.

The pulmonary blood vessels follow a series of branching tubes similar to the airways, beginning at the pulmonary arteries to the capillaries and then continuing back up to the pulmonary veins. The arteries, veins and airway bronchi initially run alongside one another, but toward the peripheral region of the lung the veins move away to pass between the lobules, while the arteries continue down the center. The capillaries that cover the alveoli become the terminal meeting point for the arterial and venous blood supply as depicted in Figure 2.4. Each capillary is roughly 10µm in diameter, which is just large enough for a red blood cell to pass through. The capillary network surrounding the alveoli is so dense it practically forms a continuous sheet of blood, which makes for a very efficient gas exchange structure. While the pulmonary arteries receive all of the output from the right side of the heart, the resistance in the pulmonary system is so small that the mean pulmonary pressure is only about 20 cmH_2O providing a flow rate of 5-6liters/min [27]. Figure 2.5 provides an illustrative depiction of the balance between ventilation and perfusion through a normal human lung.

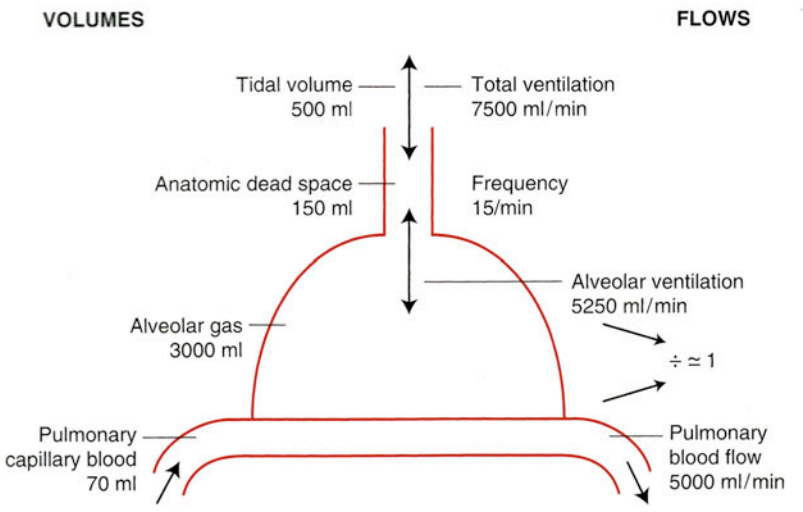

Figure 2.5: Schematic of ventilation and perfusion through the human lung, [9].

2.1.4 Defense Mechanism

As described, the lung has an enormous surface area for gas exchange. Since the airways are almost directly exposed to the atmosphere and indirectly to the circulating blood, the lung is extremely vulnerable to foreign particles. The lung has multiple defense mechanisms in place to maintain a warm, humid and clean environment in the airways. In the upper airways, the nasal cavity traps large particles greater than 10μm through a collection of irregular structures and the secretion of mucus. In contrast, the conducting airways trap and move foreign particles (5-10μm) up into the throat via a complex mucociliary escalator system where they are swallowed or coughed out. Coughing and sneezing are two reflexes that the lung also uses to evacuate the airways and nasal cavity from trapped particles. Finally, the alveoli are home to phagocytic macrophages, which engulf particles smaller than 2μm entering the respiratory zone. Since the velocity of the air at the respiratory zone is practically zero, small particles often settle there. Macrophages engulf such particles and either move up towards the conducting region where they are transported out of the lung via mucociliary clearance or are removed from the lung via the lymphatic or circulatory systems. The lung also has a complex immune system not detailed here that is activated through the interaction of foreign particles with macrophages, T- and B-lymphocytes [27].

2.1.5 Conclusion

In this section an overview of the basic lung structure and function has been given. The lung is primarily designed for gas exchange of oxygen into and carbon dioxide out of the blood stream, but also performs other important functions such as metabolizing some compounds, filtering of foreign particles, removing unwanted materials from circulation, and acting as a blood reservoir. As the lung is vulnerable to foreign particles, a series of defense mechanisms are in place to counteract any potentially harmful intrusion. While the lung may be perceived as a simple organ, it is quite complex and requires well-coordinated interaction between the central nervous system, diaphragm, chest wall intercostals muscles and the circulatory system. Our understanding of the lung has increased dramatically over the past hundred years, yet many facets of the true complexity and underlying mechanisms of the lung still elude us.

2.2 Microscopic Pathology Imaging

2.2.1 Introduction

Pathology is the study of disease mechanisms. The term encompasses both examinations of tissue and bodily fluids as well as clinically important information such as patient history. The concept of studying disease through examination of diseased organs, tissues and cells seems obvious today, but there are no recorded examples of autopsies prior to the second millennium, with the first postmortem dissections described by the Arabian physician Avenzoar (1091-1161), who showed that scabies was caused by a parasite. The next recorded dissection was the discovery of pulmonary circulation by Ibn al-Nafis in 1242.

While the microscope was invented in the 1600s, Rudolf Virchow (1821-1902) is considered the father of microscopic pathology since he was one of the first renowned physicians to emphasize the study of diseases through cellular observation [28]. Histology is the study of cells from a thin slice of tissue normally under a microscope. Histopathology is the study of diseased tissue using thin sections under a microscope. In modern times, with the advancement of microscopy technology as well as our deeper understanding of molecular biology and immunology, histopathology has become a vital tool in both the clinical and research setting.

2.2.2 Pulmonary Histopathology

Examination of lung tissue by histopathology is preceded by a series of procedures which include dissection, fixation, embedding, sectioning and staining. The most common sequence includes: formalin fixation, paraffin embedment, 4 μm sections onto glass microscope slides and Haematoxylin and Eosin (H&E) staining. This is a well-developed sequence and is the ‘gold standard’ for clinical pulmonary diagnosis of diseases such as emphysema, bronchiolitis, granuloma and lung cancer. In lung morphology research, the embedment medium is often substituted for methyl methacrylate, which is known to produce sections that are less prone to shrinkage normally associated with paraffin embedding. Light microscopy is the ‘gold standard’ for clinical diagnosis and the most common for research with other

microscopy techniques such as scanning electron microscopy and laser scanning confocal microscopy, utilized for high magnification structural examination.

Comparison of non-invasive imaging techniques with pathology is an important area of research as it relates clinical imaging techniques to their 'ground truth' histology. Currently, relating histopathology to non-invasive three-dimensional imaging techniques such as CT, MRI and ultrasound, is performed in a very subjective manner. Attempts to accurately correlate the two have been problematic since tissue samples are either acquired at biopsy, with very minimal knowledge on the spatial correlation to the organ as a whole, or whole organs are sectioned into smaller pieces for histological processing, with spatial information largely lost in this translation.

The single greatest hurdle for correlating pulmonary histopathology to non-invasive imaging techniques has been the method of lung fixation. To date, no one technique has met the individual needs of the majority of pulmonary researchers. The problem relates to the inherently delicate structure of the lung and the requirement to recapture its morphology as close to its living state while preserving cellular integrity. Initial techniques with air-drying produced a brittle end product with unsatisfactory histology. Techniques then evolved to formalin fixation as formalin became more commonly used in the early 1900s as a fixative [29]. With such fluid fixation, subsequent radiological examination was impossible as the lung appeared to be drowned. Formalin instillation techniques then evolved into formalin vapor fixation and, depending on the protocol, produce well-fixed lung tissue with minimal shrinkage and potential for use in radiographic comparison. This was not widely adopted as vapor fixation required a complex setup of apparatus. In 1962 Sills [30] proposed a new technique that was based on replacing the water content of the lung with Glycol; the fixation was performed with inclusion of ethyl alcohol and formalin. This new method produced very high quality whole lung specimens that were spongy, dry but not brittle. Thin sections could be obtained from the specimen and both radiographic and histological examinations were of high quality. The technique was simplified by Heitzman [31] and provided a similar end product that could be used for photographic, histopathologic and radiographic examination. When published, this new technique had already been well tested and successfully

used for storing fixed lungs for over 10 years with good histopathology despite the prolonged storage [31].

An example of a sheep lung fixed in our laboratories using the Heitzman technique is shown in Figure 2.6.

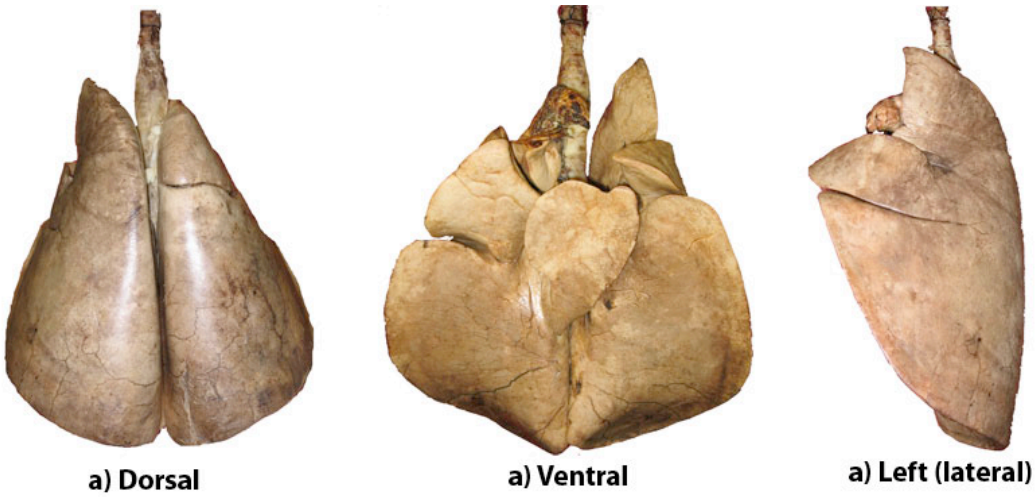

Figure 2.6: Sheep lung fixed using the Heitzman technique, a) dorsal, b) ventral and c) Left lateral view.

2.2.3 Conclusion

Pathology is now a vital discipline in pulmonary disease management and research. While many pathology techniques developed over the last fifty years are still in use today, many new methods are continually investigated and translated into the clinical setting. One major advance in research that has made great strides in the understanding of lung structure and function is the development of fixation techniques that better preserve the macro and microstructure of the lung. Utilizing these new techniques, correlation of lung pathology with non-invasive imaging systems such as chest X-ray, computed tomography and magnetic resonance imaging has become a realistic goal.

Finally, while great strides in lung pathology have taken place to date, imaging the lung at the cellular level has only been accomplished on fixed specimens representing a static point in time. If we are to better understand the underlying

microscopic structure and function in the living-breathing lung, new dynamic imaging techniques are needed.

2.3 Micro-CT Imaging

2.3.1 Introduction

X-rays were discovered in 1895 when the German physicist, Wilhelm Conrad Röntgen noticed a green fluorescent "glow" coming from a screen sitting close to a cathode ray tube he was working on [32]. After some experimentation he found that this new form of light or ray was capable of passing through most substances and produced a shadow on pieces of film. He named this new ray X-ray as "X" in mathematics is used to identify an unknown quantity. In 1901 Röntgen was awarded the first Nobel Prize in Physics for his achievement of producing, detecting and documenting X-rays [33].

In 1917 Johann Radon published formulae that would later solve the reconstruction problem relating one-dimensional projections to two-dimensional images through the inverse transform.

Computed Tomography owes its presence to the initial discovery of X-rays and the development of mathematical formulae to solve the reconstruction problem. Computed tomography can be generalized as a technique in which a series of two-dimensional projections acquired around a single axis of rotation are used to reconstruct a three-dimensional image of the internal structures of an object.

In 1972 Sir Godfrey Newbold Hounsfield invented the first commercial CT scanner [34]; simultaneously, Allan McLeod Cormack independently invented a similar system and both were honored with the 1979 Nobel Prize in Medicine.

X-ray imaging has played an important role in medicine since its inception when Röntgen used X-rays to identify bones. While particularly useful for identifying skeletal anatomy and pathology, X-rays have also become a key diagnostic technique for soft tissue diseases found within the pulmonary system, such as

tuberculosis, pneumonia, edema and lung cancer. The progression of X-ray projection imaging to more advanced X-ray computed tomography systems has changed the face of medicine.

2.3.2 X-ray Imaging

An X-ray is a form of electromagnetic (EM) radiation with a wavelength between 10 to 0.01nm. EM radiation is characterized by its wavelength (λ), frequency (ν), and energy (E). The speed (c), wavelength, and frequency are related by

$$c = \lambda v . \tag{2.1}$$

When EM radiation interacts with matter, it exhibits a particle-like behavior, where each packet of energy is referred to as a photon. The energy of a photon is given by

$$E = hv = \frac{hc}{\lambda}, \tag{2.2}$$

where h is Planck's constant = 6.62 x10-34J-sec = 4.13x10-18 keV-sec. When describing x-rays, photon energy is expressed in electron Volts (eV).

X-rays are referred to as ionizing radiation because X-ray photons carry sufficient energy to remove electrons from atomic shells, thereby producing ionized atoms and molecules. Ionizing radiation is harmful since it leads to the destruction of molecules in cells and DNA causing cell death or genetic mutations that can lead to health problems such as cancer.

2.3.2.1 Interactions

X-ray photons interact with matter through penetration, scattering and/or absorption. Four major interactions associated with X-rays exist, but only the first three occur in X-ray interaction in diagnostic radiology. These include Rayleigh scattering, Compton scattering, and photoelectric absorption. Pair production, the fourth type,

only occurs when photon energies are greater than 1.02MeV, far greater than the commonly 30-140keV used in clinical computed tomography.

Rayleigh scattering, also referred to as “coherent” or “classical” scattering, refers to the energy radiated from a whole atom when the incident X-ray photon interacts and excites the total atom. This occurs when the electric field of the incoming photon’s electromagnetic wave releases energy, causing all of the electrons in the interacting atom to oscillate in phase. This oscillation causes the electron cloud to immediately radiate energy as an emitting photon. Ionization does not occur because no electrons are ejected. Since the scattering angle of the emitting photon increases with a decrease in incoming X-ray energy, the detection of these scattering photons is problematic in medical imaging and produces artifacts in the detected image. It should be noted that the occurrence of this type of interaction is low in the normal energy range of diagnostic radiology, with the exception of soft-tissues imaging, where Rayleigh scattering may cause artifacts due to energies of less than 30keV [35].

Compton scattering also referred to as “inelastic” or “non-classical” scattering, is the primary interaction of X-rays with soft tissue in diagnostic radiology. This interaction is thought to occur predominantly with the outer shell electron. Here, the X-ray photon is scattered with a lower energy after ejecting an electron from the outer shell. Since an electron is ejected, Compton scattering results in ionization of the atom. The scattered photon can then continue through the medium with or without further interactions not limited to Compton scattering.
The greater the energy of the incident X-ray photon, the straighter and less deviated is the photon and electron scatter. For projection X-ray imaging this is important since photons that remain in the forward direction will more likely be detected. This reduces image contrast since there is less attenuation of the primary X-ray photon due to differences in the tissue densities. The incident X-ray photon energy must be greater than the binding energy (the energy required to free electrons from their atomic orbits) of the electron for a Compton interaction to occur. The likelihood of this interaction increases as the incident photon energy increases as compared to Rayleigh scattering or photoelectric absorption (discussed below). The probability of Compton scattering is also related to the electron density; with the exception of

hydrogen, the total number of electrons/g is practically constant in tissue and does not effect the probability of this interaction in medical imaging [35].

In the photoelectric effect, the incident X-ray transfers all of its energy into an electron that is ejected from the atom, and therefore the incident X-ray energy must be greater than or equal to the binding energy of the electron. The electron that is ejected is normally the one whose binding energy is nearest, but less than the incident X-ray photon. For atoms with high atomic numbers having multiple electron shells, the interaction can cause a cascade effect of vacancy electrons being filled by lower binding energy shell electrons. This produces characteristic X-rays at each electron drop. The occurrence of this process is limited in soft tissue imaging where the atomic numbers are relatively low.

2.3.2.2 Source

X-rays are produced when fast moving electrons interact with matter, normally a dense metal target such as tungsten, and transform their kinetic energy into electromagnetic (EM) radiation. A schematic example of an X-ray source is shown in Figure 2.7. By heating the cathode filament, electrons are emitted from its surface. A large voltage is then applied between the cathode and the anode, such that the anode's positive charge attracts and accelerates the negatively charged electrons towards it. The kinetic energy gained through the acceleration is proportional to the potential difference between the cathode and anode. When the electrons hit the target (anode) the kinetic energy is then converted into different forms of energy. By far the greatest conversion is into heat, accounting for 99% of the energy, with emission of X-rays accounting for less than one percent. The production of heat also becomes the limiting factor in the number of photons that can be produced without damaging the anode [35].

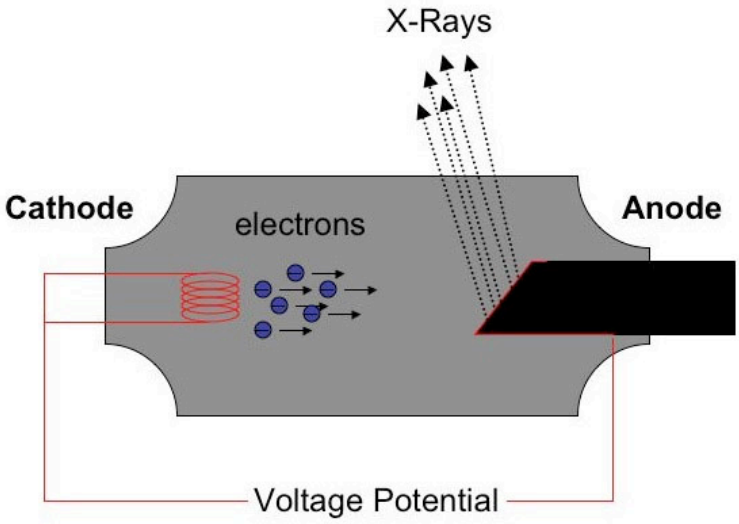

Figure 2.7: Schematic example of an X-ray source.

In micro-computed tomography the source is known as a microfocus X-ray source since the focal spot size of the emitted X-ray beam is <50µm, unlike conventional computed tomography, which has a focal spot size > 300um [36, 37].

2.3.2.3 Detectors

Detection of X-rays is normally performed indirectly through conversion of X-rays into visible light. A common technique is to place an intensifier in front of a light detector, such as a charge-coupled device (CCD) detector. A common intensifier is a fluorescent cesium iodide crystal plate, which converts X-rays into visible photons. The thicker the plate the more photons are produced. However, increasing the thickness of the intensifier also reduces the spatial resolution as the potential for stray light increases. This can also cause ghosting, where the excitation from the previous image is still present when the next image is being acquired.

The most common method of coupling the visible light emitted from the intensifier to a CCD sensor is through a tapered fiber optic.

CCDs are integrated circuits made from crystalline silicone with photosensitive discrete pixel elements. As more light falls on a photosensitive element, the number of electrons produced and the brightness of the resulting pixel output increase. Once a CCD chip has been exposed the pixels must be read. This read out process

involves shifting each charged packet down every column simultaneously. Charged packets in the bottom row are then shifted across with each packet read by the readout electronics as shown in Figure 2.8. Once the entire row is read and cleared, the process is repeated and charged packets are moved down simultaneously from every column. As one can imagine, the readout process takes considerable time and is a primary factor when designing X-ray imaging systems that require fast acquisition speeds.

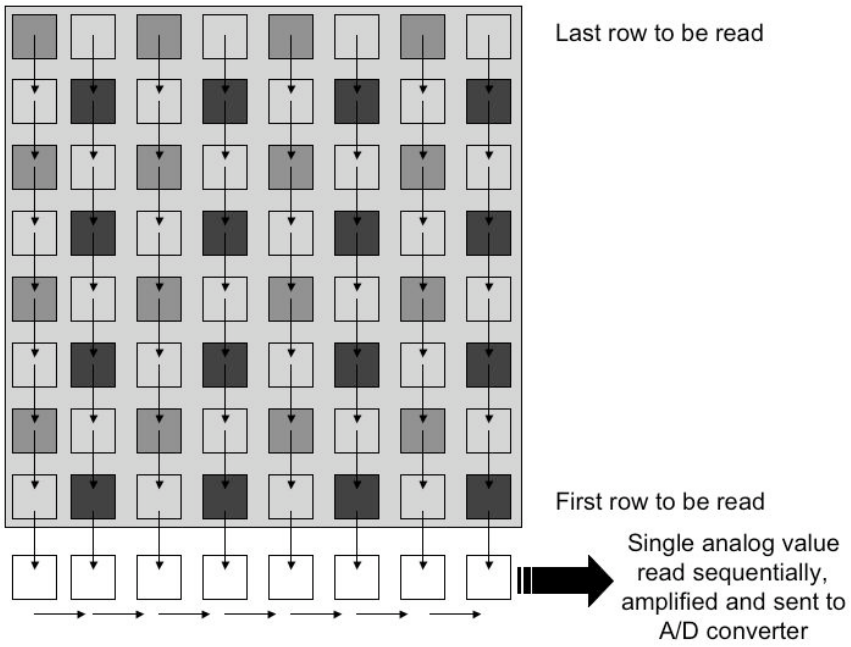

Figure 2.8: CCD readout flow diagram.

In the micro-CT system used throughout this thesis, a coherent bundle of optical fibers, tapered from a large (intensifier) to small area CCD, is used. The magnification using this method is fixed but produces a very efficient coupling.

Other detection techniques include discrete scintillation detectors, flat panel semiconductor detectors, and various image intensifier schemes. The method described above is the most common for small animal computed tomography systems and is implemented in the micro-CT system used throughout this thesis.

2.3.2.4 Attenuation

Attenuation is a result of absorption and scattering (as discussed in Section 2.3.2.1) of the incident X-ray photons as they pass through a medium. To recap, low energy

photons dominate the attenuation in soft tissue through the photoelectric effect. Compton scattering dominates when high-energy photons interact with low atomic number materials, like soft tissue. Finally, Rayleigh scattering occurs at low incident X-ray energies <30keV with a low probability of approximately 10%.

The linear attenuation coefficient (μ cm^{-1}) is the common term used to quantify the percentage of photons removed from a monoenergetic beam of X-rays through a medium of a discrete thickness. For a very small thickness Δx, the number of removed photons is expressed by

$$n = \mu N \Delta x \ , \qquad 2.3$$

where n is the number of removed photons, and N is the number of incident photons.

For an increasing material thickness the relationship is not linear and can be redefined as an exponential relationship, where the number of incident photons (N_0) and those that are transmitted (N) through a thickness x without interaction is expressed as

$$N = N_0 e^{-\mu x} \ , \qquad 2.4$$

where the linear attenuation coefficient representing the sum of the coefficients for each type of interaction is represented by

$$\mu = \mu\text{Rayleigh} + \mu\text{Photoelectric Effect} + \mu\text{Compton Scatter} + \mu\text{Pair Production}. \qquad 2.5$$

For tomographic reconstruction we can use the more familiar equation

$$I_t = I_0 e^{-\mu t} \ , \qquad 2.6$$

where I_0 is the non-attenuated intensity of the incident X-ray beam, and I_t is the X-ray intensity measured by the detector after it passes through the patient/material of thickness t. We are interested in μt, which is related to the attenuation of the patient/material. Rearranging equation 2.6 results in

$$\ln \frac{I_0}{I_t} = \mu t . \qquad 2.7$$

2.3.3 Image Reconstruction

The major advantage of Computed Tomography is its ability to non-invasively reconstruct a cross section of an object from a set of projections. In the ideal case, projections represent integrated values of the attenuation coefficient of the object along straight lines. In the following section, we will define line integrals and how they are used to form projections. We will then discuss the well-known reconstruction algorithm based on the Fourier Slice Theorem, which is derived from the Fourier transform of a projection taken along parallel lines.

2.3.3.1 Line Integrals and Projections

A line integral is the integral of some parameter, in this instance total attenuation of a beam of X-rays as it passes through tissue along a straight line. To describe line integrals and projections we will refer to the coordinate system defined in Figure 2.9.

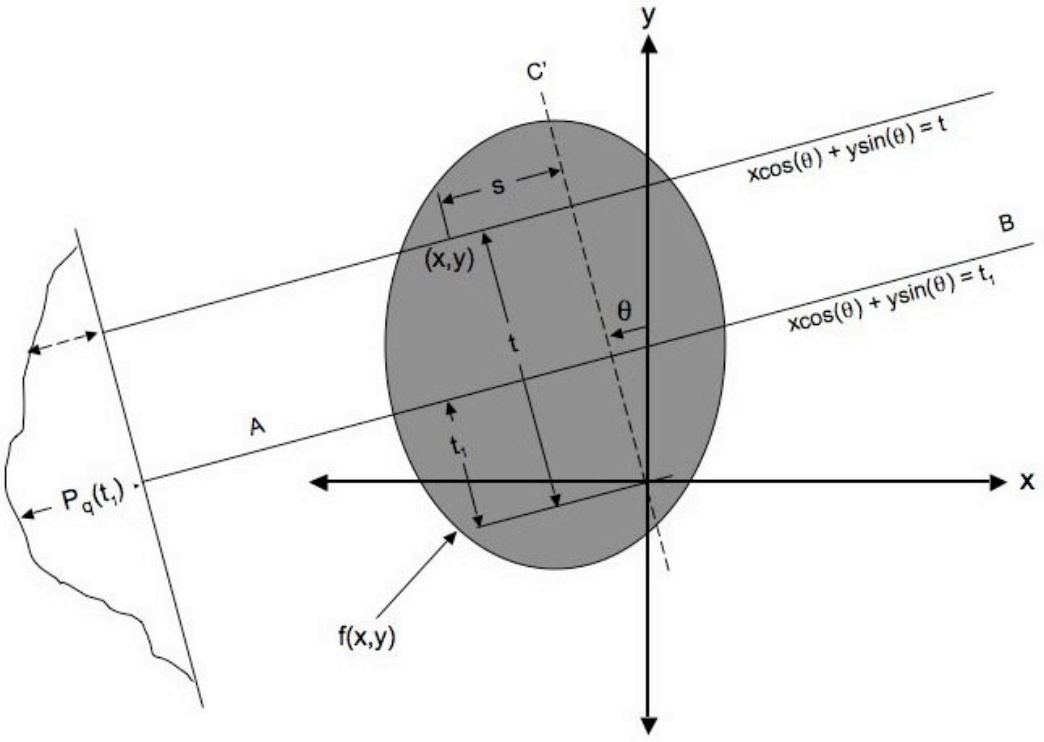

Figure 2.9: Geometry co-ordinate system, recreated from [38].

An object is a two-dimensional object with function $f(x,y)$ with each line integral represented by (θ, t). Where θ represents the angle of incidence of the ray and t represents its distance from the origin. The line AB in Figure 2.9 is represented by the equation

$$x\cos\theta + y\sin\theta = t_1. \tag{2.8}$$

The line integral is then defined as

$$P_\theta(t) = \int_{-\infty}^{\infty} f(s\cos\theta + t_1\sin\theta,\ s\sin\theta - t_1\cos\theta)\ ds\ , \tag{2.9}$$

which can be re-written using a delta function as

$$P_\theta(t) = \int_{-\infty}^{\infty}\int_{-\infty}^{\infty} f(x,y)\delta(x\cos\theta + y\sin\theta - t)\ dx\,dy\,. \tag{2.10}$$

This function $P_\theta(t)$ is known as the Radon transform of $f(x,y)$. Exact reconstruction is possible if $P_\theta(t)$ is known for all θ. In practice $P_\theta(t)$ is only available for a finite number of θ, so only approximate solutions are possible.

2.3.3.2 The Fourier Slice Theorem

The Fourier Slice Theorem relates the Radon data to a radial profile in the Fourier space, thereby allowing reconstruction of the cross sectional slice of an object. Therefore, the Fourier Slice Theorem results in a slice of the Fourier transform of the original object f(x,y), by calculating the Fourier transform of a parallel projection of the image f(x,y) at an angle θ.

We begin by defining the Fourier transform of the object as

$$F(u,v) = \int_{-\infty}^{\infty}\int_{-\infty}^{\infty} f(x,y)e^{-j2\pi(ux+vy)}dxdy\,. \qquad 2.11$$

Also, we define the Fourier transform of a parallel projection as

$$S_\theta(w) = \int_{-\infty}^{\infty} P_\theta(t)e^{-j2\pi wt}dt\ , \qquad 2.12$$

where P_θ is the projection at an angle θ.
The simplest description of the Fourier Slice Theorem is for the projection angle $\theta=0$, here the Fourier transform of the object in equation 2.11 simplifies to

$$F(u,0) = \int_{-\infty}^{\infty}\int_{-\infty}^{\infty} f(x,y)e^{-j2\pi ux}dxdy\ , \qquad 2.13$$

where $\nu = 0$ for the Fourier transform of the object shown in equation 2.11.
Now, since the phase component of y has been removed, the integral can be split into two, resulting in

$$F(u,0) = \int_{-\infty}^{\infty}\left[\int_{-\infty}^{\infty} f(x,y)dy\right]e^{-j2\pi ux}dx\,. \qquad 2.14$$

Now, from the definition of a parallel projection along the lines of a constant x is

$$P_{\theta=0} = \int_{-\infty}^{\infty} f(x,y)dy\,. \qquad 2.15$$

Substituting equation 2.15 into equation 2.14 simplifies into:

$$F(u,0) = \int_{-\infty}^{\infty} P_{\theta=0}(x) e^{-j2\pi ux} dx \ . \qquad 2.16$$

The right-hand side of the above equation represents the Fourier transform of the parallel projections at $\theta=0$; from equation 2.12 we have the following relationship between the vertical projection and the two-dimensional Fourier transform of the object f(x,y)

$$F(u,0) = S_{\theta=0}(u) \ . \qquad 2.17$$

This is the simplest form of the Fourier Slice Theorem, and is independent of the object orientation with respect to the coordinate system.

Now we can derive the equation which forms the basis for straight ray tomography by considering the (t,s) co-ordinate system as a rotated version of the original (x,y) system where

$$\begin{bmatrix} t \\ s \end{bmatrix} = \begin{bmatrix} \cos\theta & \sin\theta \\ -\sin\theta & \cos\theta \end{bmatrix} \begin{bmatrix} x \\ y \end{bmatrix} . \qquad 2.18$$

The parallel projections along lines of constant t are written as follows in the (t,s) coordinate system

$$P_{\theta}(t) = \int_{-\infty}^{\infty} f(t,s) ds \ . \qquad 2.19$$

Substituting equation 2.19 into 2.12 gives

$$S_{\theta}(w) = \int_{-\infty}^{\infty} \left[\int_{-\infty}^{\infty} f(t,s) ds \right] e^{-j2\pi wt} dt \ . \qquad 2.20$$

Using the relationship defined in equation 2.18, we can transform back into the (x,y) co-ordinate system as

$$S_\theta(w) = \int_{-\infty}^{\infty}\int_{-\infty}^{\infty} f(x,y)e^{-j2\pi w(x\cos\theta + y\sin\theta)}dxdy \ . \qquad 2.21$$

The right-hand of this equation represents the Fourier transform f(u,ν) as in equation 2.11 at a spatial frequency, where u=wcosθ and ν=wsinθ i.e.

$$S_\theta(w) = F(w,\theta) = F(w\cos\theta, w\sin\theta) \ . \qquad 2.22$$

Therefore, by taking the Fourier transform of the parallel projections of an object f(x,y) at angles $\theta_1,\theta_2,\ldots\theta_k$, we can determine F(u,ν) on the radial lines shown in Figure 2.10.

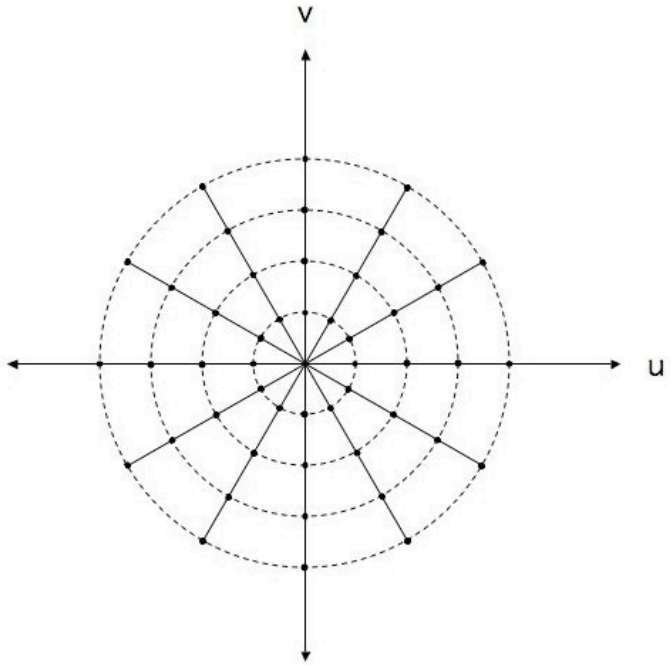

Figure 2.10: F(u,ν) the Fourier transform of the object f(x,y) along radial lines attained through projections of the object at discrete angles, recreated from [38].

If an infinite number of angles were calculated, then F(u,ν) would be known for all values of the u,ν plane. From this we can determine the original object f(x,y) by calculating the inverse Fourier transform

$$f(x,y) = \int_{-\infty}^{\infty}\int_{-\infty}^{\infty} F(u,v)e^{-j2\pi(ux+vy)}dudv \, . \qquad 2.23$$

In practice only a finite number of projections are obtained, and interpolation is performed between radial points. Also, points become increasingly sparse as they move away from the center and interpolation errors become larger for high frequency components in the image.

2.3.3.3 Filtered Back Projection

The Fourier Slice Theorem provides a nice theoretical model of tomographic reconstruction, but in practice for computer implementation, the filtered back projection algorithm is most commonly implemented. The filtered back projection algorithm can be derived from the Fourier Slice Theorem and provides for an accurate, fast and computationally efficient implementation.

Filtered back projection contains two main steps as the name implies. The first is a filtering operation that performs a weighting on each projection in the frequency domain, and the second, a backprojection step, which attempts to reconstruct the object from the weighted projections.

The backprojection process is demonstrated in Figure 2.11 where the original cross sectional image is shown in Figure 2.11 (a), and then reconstruction of this image using 4, 8 & 16 parallel projections is shown in Figure 2.11 (b), (c) & (d), respectively. This figure illustrates that the number of projections is directly related to the quality of the reconstructed image.

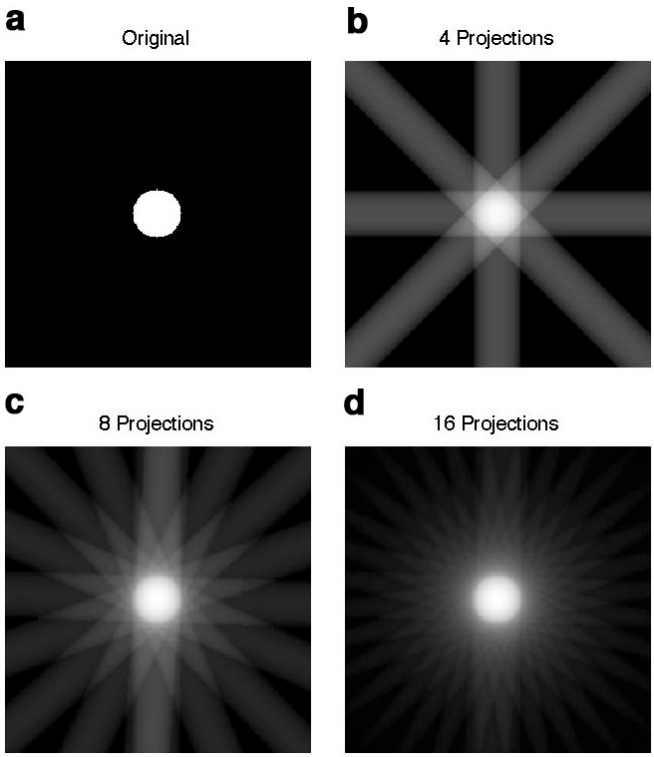

Figure 2.11: Comparison of reconstruction with 4, 8 & 16 projections.

Here the filtering has not been performed and a distinct blurring can be seen in the images. The pre-filtering step involves convolving the projection data with a filter kernel, satisfying the solution to the inverse Radon and Fourier Slice Theorem. There are many commonly implemented filter kernels used depending on the application, i.e., for soft tissue or bone imaging. The three most common filter kernels used in computed tomography: Shepp-Logan, Ram-Lak and Hamming are shown in Figure 2.12 in the frequency domain.

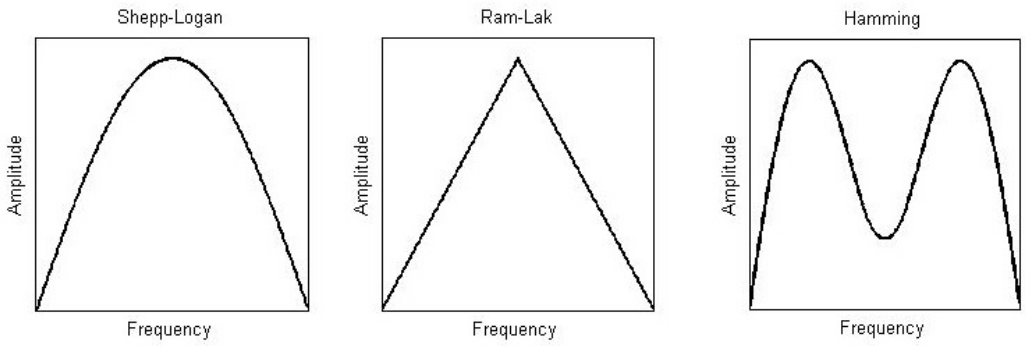

Figure 2.12: Shepp-Logan, Ram-Lak and Hamming convolution filters, where zero frequency is at the center of the x-axis.

The filtered projection data is represented by

$$P_\theta(t)' = P_\theta(t) \otimes k(t) \ , \qquad 2.24$$

where *k(t)* is the filter kernel in the spatial domain, and $\otimes$ is the symbol for convolution. Convolution is normally performed in the frequency domain since convolution in the spatial domain becomes multiplication in the frequency domain. In the frequency domain equation 2.24 becomes

$$P_\theta(t)' = FT^{-1}\left\{S_\theta(w) \times FT\left[k(t)\right]\right\} \ . \qquad 2.25$$

Recalling from equation 2.12, $S_\theta(w)$ is the Fourier transform of $P_\theta(t)$; also, FT represents the Fourier transform, and FT^{-1} is the inverse Fourier transform.

In this thesis, the back projection algorithm is used in combination with the "Shepp-Logan" filter. Depending on the situation, either a commercial implementation of the algorithm (Cobra, EXXIM Computing Corp., California) or a custom written Matlab (Mathworks Inc., Natick, Massachusetts) program is used to reconstruct micro computed tomography projections.

2.3.3.4 Fan beam

The theory discussed in the preceding sections was based on parallel projection data as shown in Figure 2.9. In practice, the time taken to acquire parallel projections by performing a linear scan across the projection width for each angle is too long. A much faster approach is using a fan beam to generate the line integrals. Here, a point X-ray source can be used to project attenuation signals on a single array of detectors. This fast acquisition process comes at a price and now requires a weighted backprojection algorithm. An alternative is the implementation of a fast re-sorting algorithm to transform the fan beam projections into equivalent parallel beam projections. Further detail can be found in [38].

2.3.3.5 Radial and Circumferential Resolution

The resultant back projected image has two primary resolution variables, the radial and circumferential resolution. The radial resolution is related to the source and detector resolution as well as any geometry errors. On the other hand, the circumferential resolution is based predominantly on the number of projections that are used to reconstruct the image. Depending on the application, a trade off must be made between resolution, dosage and time in order to produce the highest image quality dataset.

2.3.4 Micro Computed Tomography

With the advent of small animal research, there has been an increasing need for imaging techniques, which are analogous to the clinical setting. Hence, micro systems for MRI, PET and CT have been developed and are becoming increasingly used for small animal research [39, 40].

Micro-CT imaging is a miniaturized computed tomography system. The hardware and software is similar to clinical CT, with several distinct differences that give rise to alternative imaging approaches.

Micro-CT systems come in various configurations, ranging from high resolution *ex vivo* imaging to fast small animal *in vivo* imaging. Initial micro-CT systems designed for imaging samples *ex vivo* / *in vitro* were setup in such a manner that the object rotated around the center of rotation rather than the X-ray source and detector as is the case in clinical CT. This setup allows for accurate modeling of the geometry and provides the highest resolution images (<10 microns). Recently, *in vivo* systems have been developed and commercialized to more closely mimic clinical CT systems where the source and detector rotate about the object as shown in Figure 2.13. In the *in vivo* situation, acquisition times need to be at a minimum and hence the X-ray source is generally more powerful than those found in the *ex vivo* systems. The increase in X-ray power is related to the effective focal spot size resulting in lower resolution images in the order of 40-100microns.

In the majority of commercial micro-CT systems, the detector is a large two-dimensional matrix. This setup captures the entire field of view with one projection, as opposed to a single row of detectors spinning around a moving bed, resulting in a spiral scan - as is the case in current clinical CT systems. In this case, it is not necessary to move the specimen bed forward during scanning as performed in spiral CT.

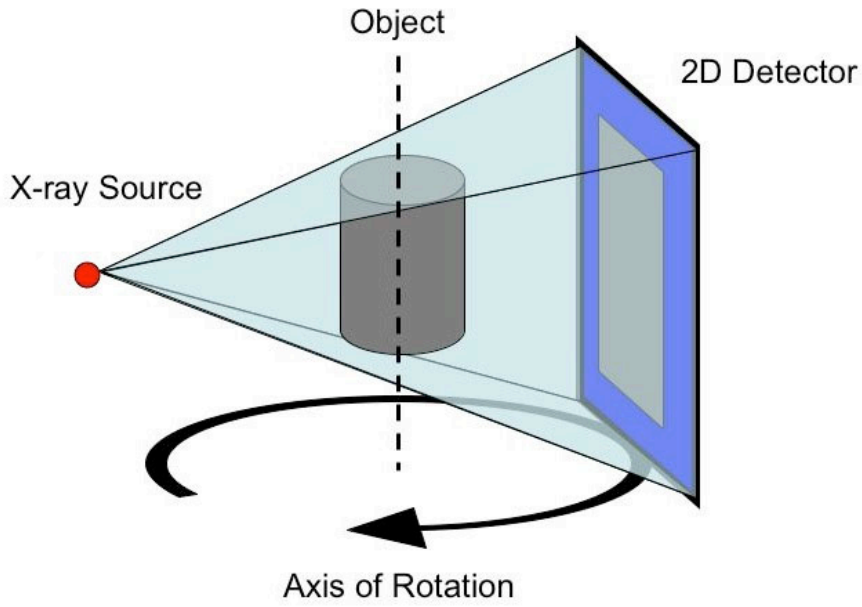

Figure 2.13: Typical micro computed tomography cone-beam geometry.

With a two-dimensional detector the projection ray is no longer a fan beam but instead is a cone beam, requiring a different reconstruction algorithm posing new obstacles. The most commonly implemented reconstruction algorithm for micro-CT imaging is the Feldkamp cone-beam algorithm [41].

2.3.4.1 Ring Artifacts

In third generation clinical CT systems, the detector and source spin around the object coincidently, and each detector element represents the same radial pattern in the reconstructed image. Ring artifacts are a result of adjacent detector-detector differences, which produce either dark or light circles in the reconstructed images. This problem has been eradicated in fourth generation clinical CT systems where the

source spins around the object, and there is a stationary ring of detectors covering the entire radial field of view.

In the majority of micro-CT systems, each detector element represents the same position between projections. Errors in sensitivity between adjacent elements become enhanced through the back projection process as these errors are superimposed on the same radial position. An example illustrating ring artifact from a micro-CT system is shown in Figure 2.14.

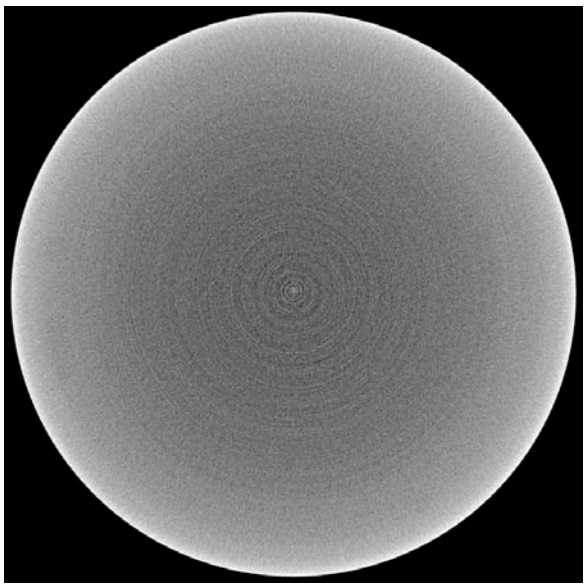

Figure 2.14: Ring artifact example from a micro-CT water phantom scan.

2.3.4.2 Beam Hardening Artifacts

Also in Figure 2.14 is the clear depiction of beam hardening artifacts i.e. the change in X-ray attenuation across an otherwise homogenous water phantom. This is a common problem when using a polychromatic X-ray source in a micro-CT system where attenuation of X-rays is no longer a linear function of the object thickness. Such nonlinearities must be addressed prior to quantification of reconstructed images, as attenuation values will otherwise be incorrectly determined. This is of particular importance in *in vivo* pulmonary imaging where structural changes that are beyond the resolving capacity of the scanner, such as alveolar size, can be indirectly assessed using the change in gray scale attenuation values. This does not

give a true representation of alveolar size, but can provide a good indication of the tissue/air content, within the limits of the scanner density resolution.

2.3.4.3 CT numbers of Hounsfield Units

In medical X-ray imaging, attenuation values representing each pixel are normalized and truncated into integer values by the following expression:

$$CT(x,y) = 1000 \times \frac{\mu(x,y) - \mu water}{\mu water}, \quad 2.26$$

where μ(x,y) represents the high precision floating point attenuation number for each pixel (x,y) before conversion. CT(x,y) is the CT number in Hounsfield units. μwater is the attenuation coefficient for water. Once applied to the reconstructed images, the CT numbers will typically range between -1000 to 4000 Hounsfield units, where -1000 corresponds to air and water as 0.

Attenuation values are converted into CT numbers for standardization across different scans, both on the same scanner and across scanners, and are important since attenuation values are different for different X-ray energies. Hence, calibration of the CT number must be performed for different X-ray energies, and in practice is performed for every protocol, including X-ray energy, current, source-to-detector distance, filters and reconstruction grid.

2.3.5 Conclusions

In this section, an introduction of X-ray imaging with particular emphasis on the components and theory behind micro-CT has been given. The hardware for generating X-rays, detecting attenuated X-rays as well as algorithms for reconstruction of the projection data have also been briefly discussed to help reveal potential roadblocks when performing micro-CT for quantitative biological imaging, with particular emphasis on *in vivo* imaging.

Since micro-CT systems are relatively new in terms of *in vivo* imaging with the majority focused on bone samples, commercial products are still far from turnkey.

Therefore, each application requires customization and unique solutions. In this thesis, we present several novel techniques implemented on a commercial micro-CT system in order to reliably acquire data in a longitudinal study of the pulmonary system.

2.4 Laser Scanning Confocal Microscopy

2.4.1 Introduction

Laser Scanning Confocal Microscopy (LSCM) has become a common tool in biomedical research and found many applications in microscopy related fields. The advantage of confocal microscopy is its ability to create sharp images of thick specimens through its unique optical sectioning ability, which results in sub-surface images acquired without destructive sectioning. This is achieved through exclusion of light outside the focal plane of the objective.

The confocal microscope was initially developed by Marvin Minsky in 1955 and later patented in 1961 (see Figure 2.15) while he was a postdoctoral student at Harvard University [42, 43]. Marvins invention revolved around the concept of illuminating and detecting one point in the specimen at a time and using a point scanning technique to acquire a two dimensional image. This approach reduced the scattered light that would otherwise obscure an image when the whole specimen was illuminated and provided a means for imaging a focal plane beneath the surface of the specimen.

Minsky's invention went largely unnoticed, likely due to the lack of high energy light sources and the computing power required to reconstruct the large point scanning data sets. It was not until the 1970's and 80's that advances in laser and computing technology led to a resurgent interest in confocal microscopy. By the time Minsky's patent had expired, several investigators had developed their own confocal microscopes and through the development of image formation theory and demonstrated applications in biological specimens; the first commercial system appeared in 1987.

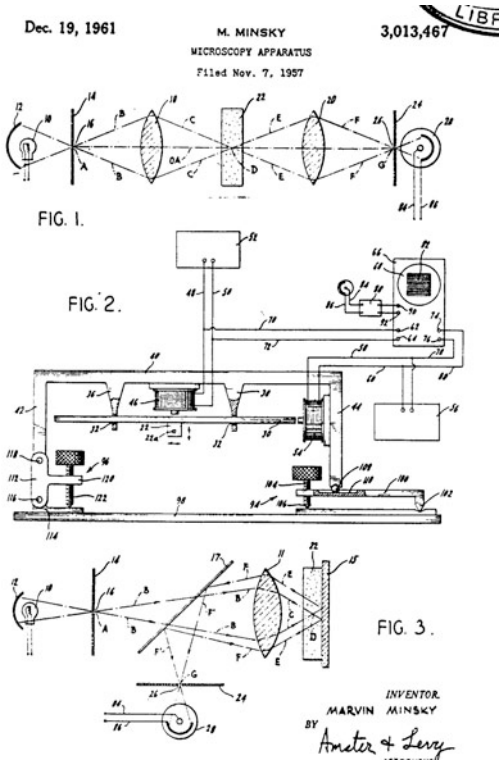

Figure 2.15: Marvin Minsky's 1961 Confocal Microscope patent.

The confocal microscope has several advantages over conventional light or epi-fluorescence microscopes, including depth of field control, reduction of background noise, and the ability to acquire optical sections that can then be reconstructed in three dimensions. The majority of commercial confocal systems use the principle of fluorescence where light of a lower wavelength is used to excite a fluorophore that emits light of a higher wavelength. This approach allows highly sensitive imaging through binding of specific tissue, cells or molecules with single or multiple color fluorophores. Confocal microscope systems are now used for routine microscopy investigation and are available in many academic centers. Other techniques include reflectance and transmission confocal microscopy, which are very similar in design and concept but are not reliant on fluorescent emission [44].

2.4.2 Confocal Microscopy

2.4.2.1 Layout

The aim in confocal microscopy is to limit the excitation and emission within the focal plane of interest. This is achieved through spatial filtering where two

conjugate focal planes are set up, one at the specimen and a second at the detector. A pinhole aperture is placed in front of the detector, constricting the light detected to a single point within the focal plane. To further reduce excitation of light from out of focus planes, a pinhole is also placed in front of the light source. In this manner only a single point in the specimen focal plane is illuminated and detected. The name confocal comes from the conjugate focal points used to spatially filter the light.

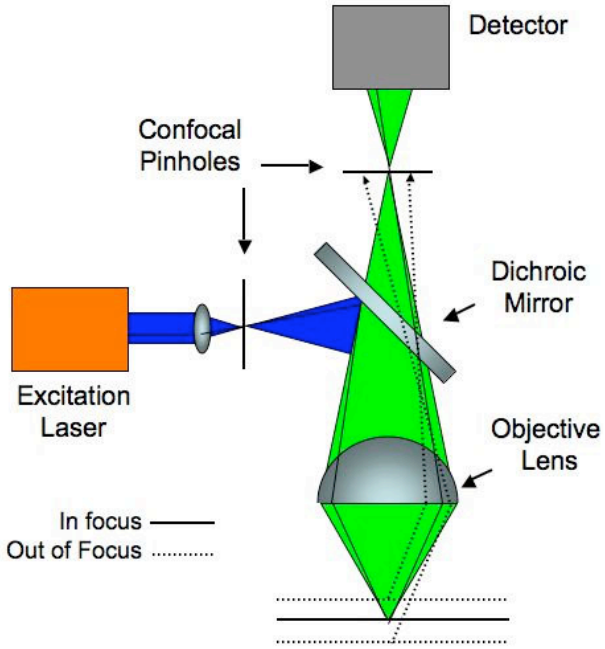

Figure 2.16: Simplified confocal microscope schematic diagram [45].

A dichroic mirror is placed between the excitation and emission arms of the system in order to separate the excitation and emission light. The dichroic mirror reflects light coming from the excitation source below a specified wavelength and transmits light from the specimen emission greater than a specified wavelength. The spatial position of fluorescence emission at the detector pinhole remains constant with only changes in intensity detected over time as the specimen is scanned. Figure 2.16 represents a simplified confocal microscope with a confocal pinhole in front of the detector and laser source along with a dichroic mirror to split the excitation and emission light.

2.4.2.2 Scan Head

The confocal microscope uses the concept of point-scanning illumination and detection of the specimen to acquire a two or three-dimensional image. In the original system developed by Minsky, the optical train was stationary and only one point was illuminated and detected. Here, the stage would move through a raster sequence to acquire a two dimensional image of the specimen. In modern systems, fast scanning mirrors are placed prior to the objective lens, scanning the specimen in the x and y direction on a stationary stage with vertical displacement in the stage used to change the focal plane.

Two mirrors are commonly utilized for the x-y scanning, one that scans the specimen from left to right along the x-axis and a second mirror to translate the horizontal scan in the y-axis. The frame rate is normally limited by the speed of the x-axis mirror, which must oscillate back and forth for every line in the frame. Since the speed of the mirrors is very slow compared to the speed of light, the excitation and emission of light at the specimen for each point follows an identical light path. A common double galvanometer mirror-scanning configuration is shown in Figure 2.17.

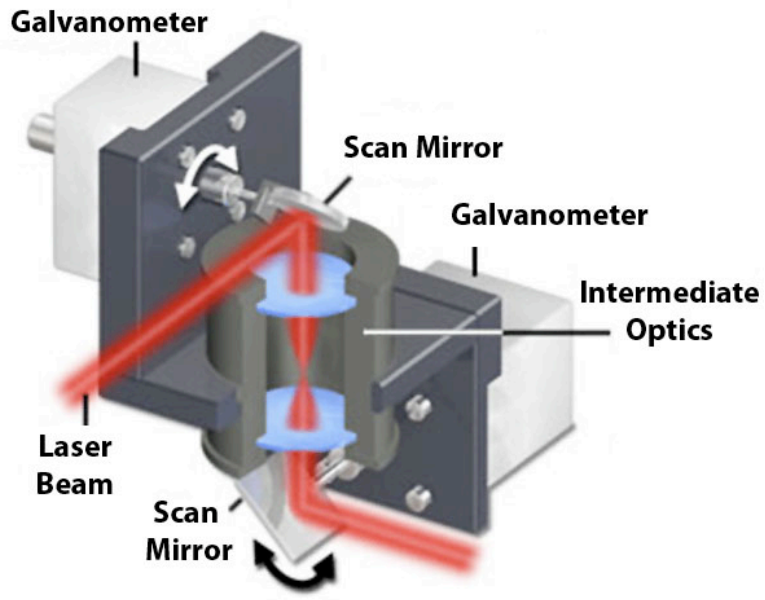

Figure 2.17: Two dimensional galvanometer scan head, modified from [46].

2.4.2.3 Laser Source

Laser light sources are now available in a wide variety of wavelengths and power outputs, and are used in commercial confocal microscopes. The laser illumination is first expanded to fill the rear aperture of the objective in order to produce a very small spot size in the focal plane as shown in Figure 2.16. Determination of the confocal spot size depends on the wavelength, objective, scanning unit and the specimen. A balance between illuminating the point of interest and reducing excess excitation around the point is desired. The most common laser source used in confocal microscopy is the Krypton-Argon gas laser, which provides the commonly used wavelength of 488nm along with two other common lines at 568 and 647nm, which can be isolated using emission filters or recently implemented Acousto-Optical Tunable Filters (AOTF).

Recently, advancements in solid-state technology have led to Double Pumped Solid State (DPSS) lasers, which are now available at multiple wavelengths including 488nm. These DPSS lasers are much smaller in footprint and do not need the same cooling requirements as gas lasers.

2.4.2.4 Detector

Photomultipliers are the most common type of detector used in confocal microscopy systems. Photodiodes and solid-state CCDs are also used, but photomultipliers are regarded as having the greatest gain and signal to noise ratio, even though they lack the quantum efficiency found in high end CCDs as shown in Figure 2.18.

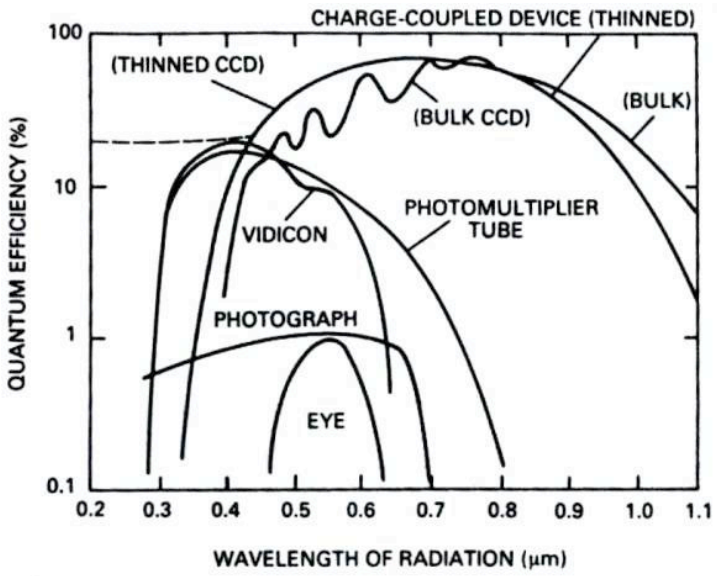

Figure 2.18: Quantum Efficiency comparison across a variety of light detecting devices, modified from [47].

Photomultipliers use a photosensitive surface to capture incident photons and produce a cascading emission of electrons through the photoelectric effect as depicted in Figure 2.19. A photomultiplier includes a vacuum tube with a photocathode window and a series of electron multipliers known as dynodes followed by an anode. The voltage between the anode and the ground is directly proportional to the photoelectron flux generated at the photocathode. A typical gain of a photomultiplier is 10^7 photons. Photomultipliers typically have a dynamic range of 10-12 bits, allowing distinction of 1024 – 4096 gray levels. The output is converted into a digital value using a high-speed analog-to-digital (A/D) converter.

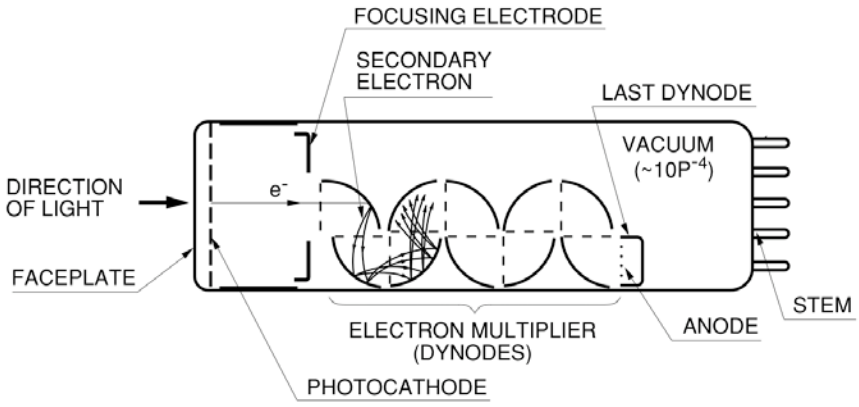

Figure 2.19: Photomultiplier schematic diagram, modified from [48].

In commercial confocal microscopy systems, multiple photomultipliers are used in parallel to simultaneously acquire images over different spectral regions. In this manner, images can be reconstructed representing different color fluorophores emitted from the specimen at the same location. Utilizing this technology, high resolution, high-quality, descriptive images of the specimen of interest are acquired with each color potentially representing a different cellular or sub-cellular feature.

2.4.2.5 Image Formation

Since laser scanning confocal microscopy is a point-by-point imaging technique, intensity values acquired from the detectors over time must be stored and reconstructed onto a two or three-dimensional grid. With the advancement of computing power over the past two decades, this is no longer a limitation of the speed of acquisition and confocal systems are now more commonly referred to as digital or video imaging systems. Depending on the scanning unit, raster scans of different width and height or, more recently, complex two-dimensional shapes can be created.

2.4.2.6 Fluorescent Probes

In biological imaging, LSCM is most commonly employed using fluorescence. Here, its utility is heavily determined by the availability of fluorescent probes for analyzing structures of interest.

Since detection of fluorescence emission can be achieved at sub-diffraction limited resolution, fluorescence LSCM provides a high degree of sensitivity and, with the appropriate fluorophore, can also be highly specific. Fluorescent probes can be used to localize specific structural regions such as the nucleus, endoplasmic reticulum, cytoskeleton and mitochondria through organic chemicals designed to bind to specific macromolecules, such as proteins. They can also be used to asses local environmental variables such as ion concentration, pH and temperature [49].

Fluorescent probes have been used since the 1800's, but they did not gain wide use in microscopy until the 1920's and further elevated in the 1940's when antibody

labeling had been developed, leading to the field of immunohistochemistry. In recent times, the discovery of green fluorescent protein (GFP) has also expanded the development of non-invasive probes used in sub-cellular localization, intermolecular interactions, trafficking in living tissue and activation of genes. There are now thousands of probes available; however, very little is still known about the molecular design rules resulting in different absorption and emission spectra. In conjunction with the limited availability of laser wavelengths on confocal microscopes, only a small subset of these probes is widely used.

A common problem associated with organic probes is dye saturation where constant irradiation with a high-energy focused laser exceeds the emission decay and results in no emission of light. This is a condition dictated by the excited state lifetime [50] and occurs when the molecule becomes saturated and the ground state population decreases. Photo bleaching, a second pathway by which a probe can lose its ability to fluoresce, is more serious and more likely to be irreversible. Photo bleaching occurs when the fluorophore permanently loses its ability to fluoresce due to chemical damage. This can occur when a fluorophore transitions from its excited singlet state to its triplet state. The triplet state is long-lived with respect to the singlet state, allowing greater time to undergo reactions that result in irreversible covalent modifications.

Quantum dots, a new type of synthetic fluorophore, are not bound by the discussed limitations, and their design rules are well understood with respect to excitation and emission wavelengths. In fact, quantum dots can be constructed with practically the same excitation spectra and distinctly separate emission spectra providing for ideal multi-label experiments. However, there widespread adoption has been limited due to their large size, i.e., approximately 10-50nm compared to 1-5nm for organic dyes [51].

A balance must then be made between the laser light intensity and the fluorescence saturation in order to achieve long life high signal-to-noise ratio in fluorescent confocal microscopy experiments [52].

2.4.2.7 Resolution and Contrast

All optical microscopes are limited in their resolution based on a set of fundamental factors. These include the numerical aperture of the optical components and the wavelength of excited and emitted light. Contrast, an important concept in imaging, is inseparable from resolution and can be defined as the minimum distance between two points that results in a specific level of contrast between them [50].

Imaging a point light source through a microscope produces an Electromagnetic (EM) field, which can be related to the response of the optical system to the input, i.e., an impulse response. It is possible to measure the intensity point spread function of a microscope by imaging a sub-resolution spherical bead. The lateral intensity distribution produces what is known as an Airy disk pattern [50]. The Airy pattern intensity is the result of the Fraunhofer diffraction of light as it passes through a circular aperture and is related to the diffraction-limiting resolution of the optical system. An example of an Airy disk pattern is shown in Figure 2.20.

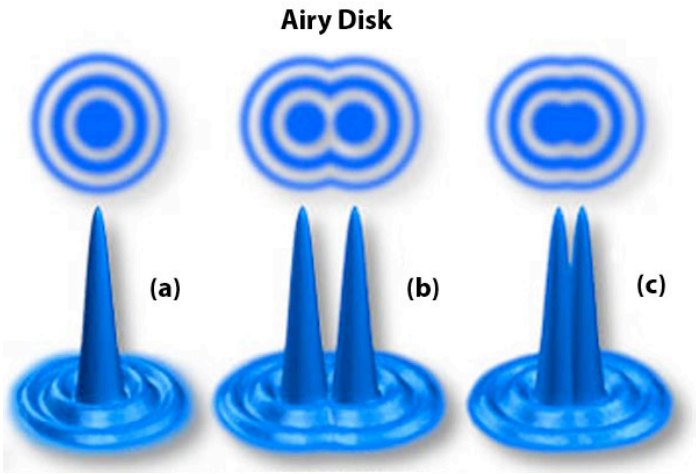

Figure 2.20: Airy disk pattern, left: top view, right: side profile, modified from [46].

The Rayleigh criterion for resolution states that two points can be resolved when the first minimum of one Airy disk is aligned with the central maximum of the second Airy disk as shown in Figure 2.20 (b). The following expression defines lateral resolution for a fluorescence microscope according to Rayleigh's criterion

$$R_{lateral} = \frac{1.22\lambda}{2 * NA} \approx \frac{0.6\lambda}{NA}, \quad 2.27$$

where lambda is the emitted light wavelength and NA is the numerical aperture of the objective.

In confocal microscopy because of the narrow intensity point spread function, the lateral resolution is reduced to an approximation of

$$R_{lateral} \approx \frac{0.4\lambda}{NA}. \quad 2.28$$

Confocal microscopy only offers a modest improvement in the axial resolution based on this equation, but the greatest advantage is the potential for optical sectioning of thick specimens.

2.4.2.8 Speed Limitations

The majority of commercial desktop confocal microscope systems acquire images between 1-5 frames per second. This is not a limitation when imaging stationary tissue samples, but with the advent of live cell and now live animal imaging, the need for video rate imaging has become apparent. The Nipkow spinning disk confocal microscope, a high-speed variant, provides fast frame rates up to 15fps. These systems are not common and have other associated limitations such as limited excitation power.

Each major component of a confocal microscope system can be the cause for speed bottlenecks [53]. The most common in modern systems is the scanning mechanism, which is a combination of galvanometer mirrors. The power of the excitation source, the sensitivity of the detector and the speed at which analog signals from the detector are digitized can all be a cause for limiting scanning speed. If these factors are resolved, there is also the limitation of the fluorophores themselves in

fluorescence confocal microscopy. Here, the excited state lifetime of a fluorophore becomes the limiting factor. Application specific solutions are commonly implemented when high-speed scanning is required and have been published by several groups [54-60]. One common solution detailed in these studies is implementation of a resonant x-axis scanner with a fixed scan speed of 4kHz+, resulting in imaging speeds of 15+ frames per second.

2.4.3 Catheter-Based Confocal Microscopy

In the last decade there has been a growing interest in developing optical techniques that can be translated into endoscopic applications. The primary motivation for translating such techniques is imaging cellular activity that resides in hollow tracts such as the pulmonary airways, colon and pancreatic duct or deep within solid organs such as brain, liver and kidney; places that would otherwise be inaccessible to conventional imaging or microscopy techniques. Laser scanning confocal microscopy (LSCM) is one such technique that has generated great interest and is now under investigation in many research labs [61-67], with several commercial systems now available [68, 69]. To be considered endoscopically viable, the end product must be no larger than the auxiliary port of a clinical endoscope in that discipline and flexible enough to get to the point of interest.

2.4.3.1 Scanning Techniques

A variety of approaches for performing the laser raster scanning normally associated with confocal microscopy for use in endoscopic systems have been implemented [70]. These approaches can be divided into two mechanisms, proximal and distal scanning.

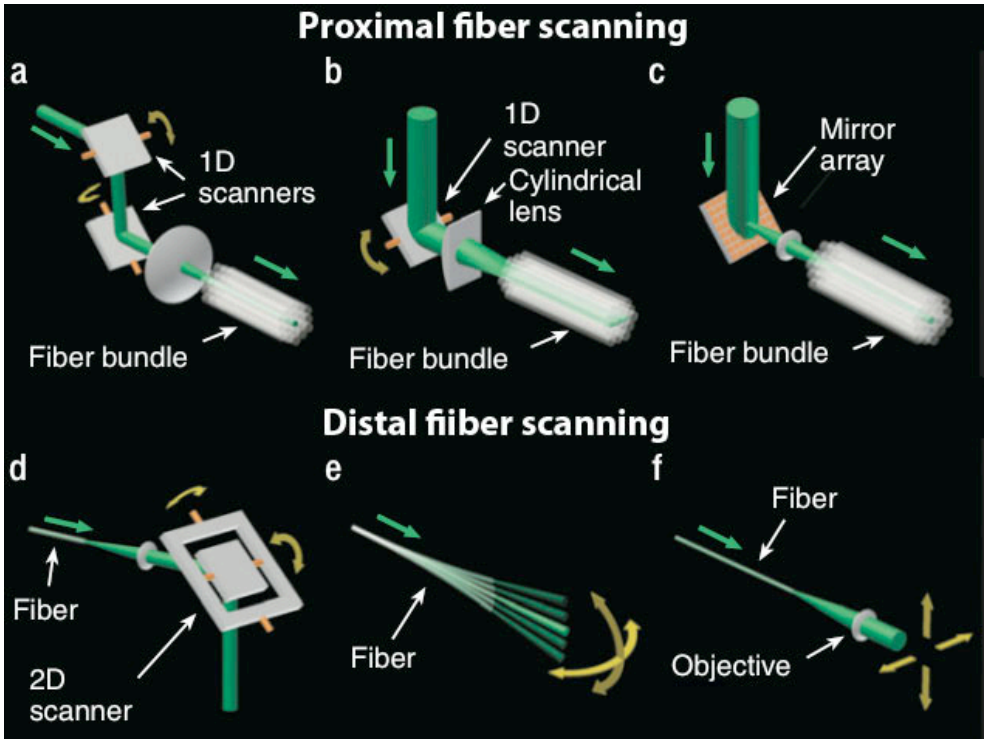

Figure 2.21: Light scanning techniques: (a-c) Proximal Scanning, (a) Cascaded galvanometer mirror couple used to scan the excitation and emission beam across the proximal end of a fiber bundle. (b) Proximal line scanning using a cylindrical lens to focus the illumination into a line, scanning the face of a fiber bundle one line at a time. (c) Proximal scanning using a spatial light modulator, which illuminates each pixel sequentially with a stationary excitation beam. (d-f) Distal Scanning, (d) Distal 2D mirror scanning using a piezo-electric mirror or a MEMS mirror setup. (e) Distal fiber tip scanning where the tip of the excitation fiber is vibrated at resonance to achieve a scanning pattern. (f) Distal fiber-objective scanning where both the fiber and the objective lens couple are vibrated at resonance. Modified from [70].

Proximal Scanning

The most common technique is scanning a fiber optic imaging bundle on the proximal end, which is coherently translated to the distal end of the fiber bundle as show in Figure 2.22. Light is then re-focused and scanned via an objective lens into the tissue matrix. This is the simplest approach since the scanning head is situated outside the 'body' or tip of the endoscope. The resolution of such systems is directly determined and limited by approximately twice the fiber-to-fiber distance divided by the magnification of the micro-objective. Several proximal scanning techniques currently exist, including cascaded galvanometer mounted mirrors (Figure 2.21 (a)) [71, 72], slit scanning with a single galvanometer mounted mirror Figure 2.21 (b) [64, 65] and finally a micro electro mechanical mirror array Figure 2.21 (c). The most common setup is the cascaded galvanometer.

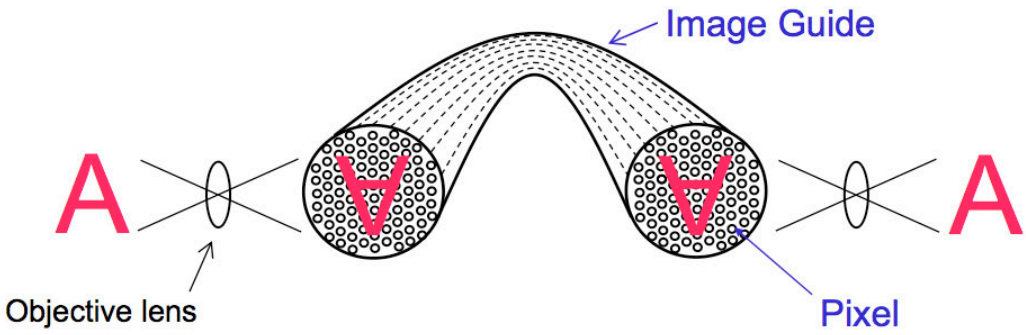

Figure 2.22: Coherent imaging fiber bundle illustration, modified from [73].

Distal Scanning

Distal scanning is technically more challenging, but possess greater potential for high-resolution imaging. There are now promising new techniques utilizing microelectromechanical system (MEMS) technology as shown in Figure 2.21 (d) to scan the tissue at the distal end of a micro-optical probe where, depending on the design, only one or two fibers are required for transmission and detection. Several groups are pioneering this technology [61-67], each with their unique design aspects. There are forward scanning [74], side scanning designs [75] and dual-axes designs [63, 66, 67]. Other distal scanning techniques include piezo electric resonant fiber scanning shown in Figure 2.21 (e) and finally resonant scanning of the fiber and objective shown in Figure 2.21 (f).

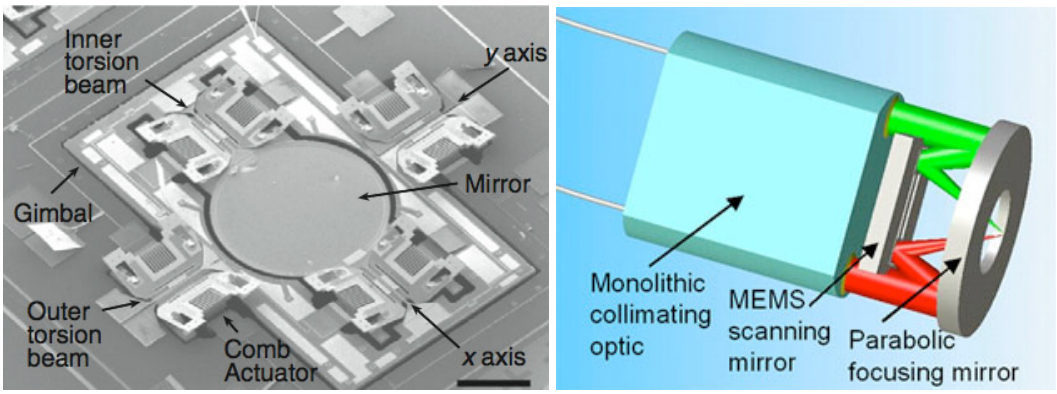

Figure 2.23: (left) Magnified view (bar equals 500μm) of a MEMS mirror [70], (right) dual-axis confocal micro-endoscope head incorporating MEMS mirror [67].

The clinical viability of these advanced and increasingly costly designs will be determined by their reliability in a clinical setting as well as their ability to be mass-produced to taking advantage of economy's of scale. In all cases, distal scanning techniques are not bound to the resolution limitations of fiber optic imaging bundle systems and with time should provide for dynamically higher resolution and field of view imaging.

2.4.3.2 Guidance and Tracking of Endo-microscopy Probes

A major clinical draw back for endo-microscopy systems is the question of where to point them, particularly in the vast pulmonary airway network. Also, the question of how to guide them to the point of interest needs to be addressed as current guidance is performed visually through the endoscope, something not necessarily possible with micro-endoscopes that can reach regions inaccessible by standard endoscopes.

Virtual bronchoscopy, a rapidly growing field, is generating great interest for micro-endoscopic pulmonary applications [76, 77]. In particular, development of electromagnetic tracking may potentially solve the localization dilemma. Virtual bronchoscopy images are most commonly generated from a CT dataset where airways have been segmented using either manual or automated techniques [78-81]. Up to now only 6-8 generations of the airways can be segmented from high-resolution CT scans in a repeatable fashion, and in the majority of cases, peripheral nodules are in the 10+ generations. Therefore, advancements in this field will also be essential if guidance of micro-optical devices is to become a clinical reality.

Figure 2.24 represents a commercial virtual bronchoscopy program (VIDA Diagnostics Inc, Iowa City, USA) with integrated path finding. Here, we can see the original CT data segmented and pseudo color-coded for lobes (a & b), a three-dimensional depiction of the airways (a & b) along with a virtual luminal view (c) at the Carina, 3rd, 5th and 8th bifurcation. The program, through interaction with the user, determines the best path to the point of interest and plans a path including anatomical instructions.

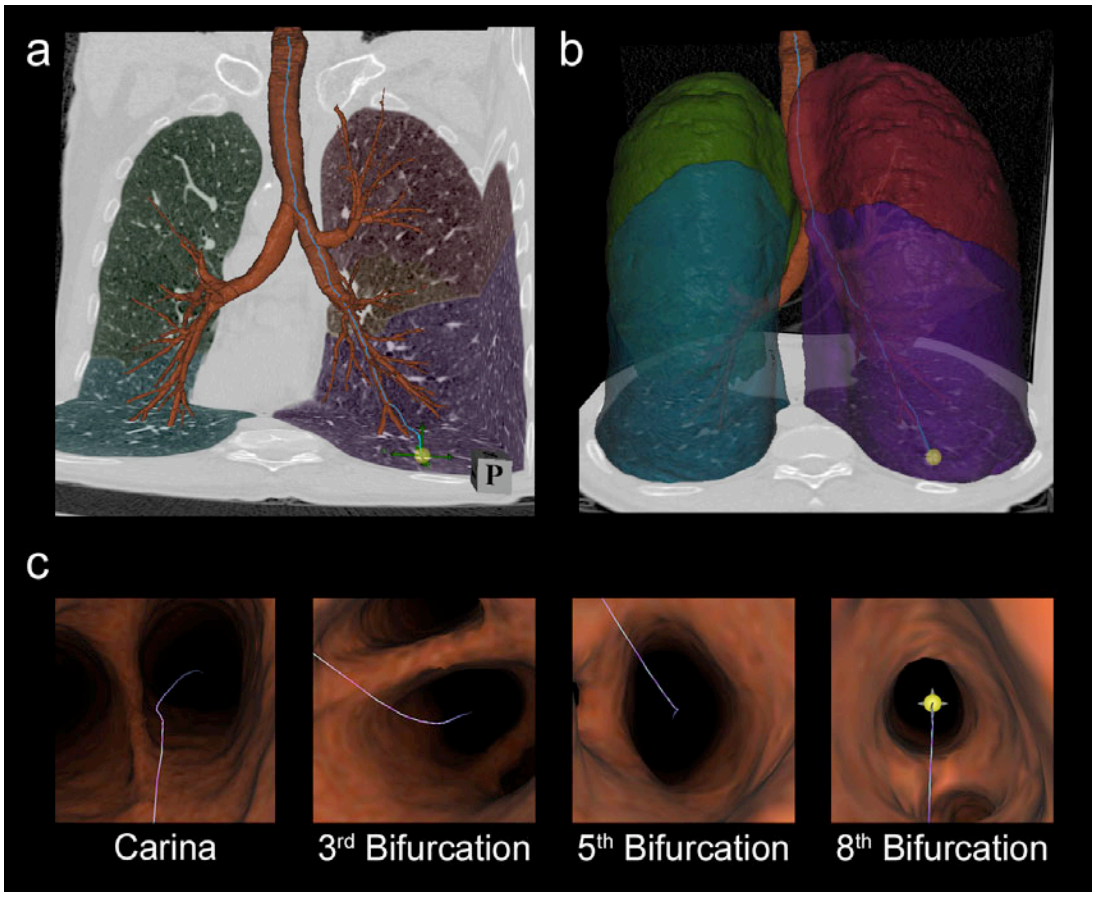

Figure 2.24: Virtual Bronchoscopy with path finding to a peripheral location.

While technical advancements are continually being made on the optical, electronic and virtual guidance frontiers, endo-microscopy systems targeted at early diagnosis of lung cancer need to be assessed on their ability to distinguish key histological and molecular changes between normal, benign, pre-malignant and malignant lesions. In particular, their ability to resolve sub-cellular structures such as nuclei in the clinical situation must be established. The success of fluorescence confocal endo-microscopy systems will thus depend largely on the availability of new and upcoming fluorescent bio-markers that will increase the sensitivity of detecting key histological structures and molecular processes that can be used for characterization of suspect sites [82].

2.4.4 Conclusions

Confocal microscopy is now used on a routine basis for investigation of cellular and molecular features in the basic sciences, something that was not possible just a

decade ago. Progress has been made from imaging fixed slide preparations, to *in vitro* cell cultures and recently to *in vivo* imaging both under bench top systems and newly developed flexible fiber-optic systems. The ability to optically section and reconstruct images in three dimensions, along with its reduced background illumination, have provided for many applications. As a fluorescence system, many new probes have emerged in the past decade, increasing the utility of confocal microscopy systems by many orders of magnitude.

In recent times, confocal microscopy has seen great interest in its ability to translate into an endoscopic tool for optical biopsy. An array of different approaches has emerged with one common goal – development of a flexible endoscopic microscopy system for real-time histological evaluation of living tissue. With the appropriate fluorescent biomarkers, an endoscopic confocal microscope system with 1-2 micron resolution could detect features in the sub-micron range through the detection of photons emitted from fluorophores bound to sub-cellular targets. Using the right strategy of imaging, biomarker tagging, endoscopic tracking and guidance, future optical biopsy approaches especially in the field of pulmonology could have a significant impact.

2.5 Mouse Models of Lung Cancer

2.5.1 Introduction

Lung cancer is the leading cause of cancer death in the world [83] with an abysmal 5-year survival rate of 16% which has seen no dramatic change over the past 30 years [84, 85]. It is set to become a worldwide epidemic with the World Health Organization estimating 10 million deaths per year worldwide by the year 2030 [85]. One potentially life saving advancement is early diagnosis and therapy; early detection is now routine with high-resolution computed tomography. However, there is a lack of viable clinical techniques for rapid *diagnosis,* which in turn has also limited our knowledge of the early underlying processes of lung cancer.

Lung cancer can be divided into two main groups: non-small-cell lung cancer (NSCLC) and small-cell lung cancer (SCLC). Approximately 80% are NSCLC and comprise of adenocarcinomas, squamous cell, bronchioalveolar, and large-cell carcinomas with adenocarcinoma and squamous cell carcinoma being the most common [86] form of NSCLC and interestingly adenocarcinomas being the most common form of lung cancer in current, former and never smokers [87].

In recent times, with the advent of the mouse genome projects [1, 2], the mouse has become the most important and commonly used research animal. There are now a multitude of mouse breeds and strains used in pulmonary pathophysiology [6, 88]. Mouse models for human lung cancer in particular have seen a recent surge of interest. These include spontaneous models in susceptible strains [89, 90], carcinogenic models [91] and genetic models encompassing transgenic techniques [86, 92, 93]. Also, there has been tremendous advancement in genetic models which carry conditional oncogene and tumor-suppressor genes allowing induction of the mutations in a timed and localized fashion [94]. These models not only advance our understanding of the underlying molecular processes of lung cancer, but also provide a unique opportunity for identifying relevant clinical biomarkers [95].

An in depth discussion of the different types of mouse models of lung cancer is outside the scope of this thesis, but a brief overview of the major types will be given

with specific emphasis on the carcinogenic Urethane model, as this is the model used within this thesis.

2.5.2 Spontaneous and Carcinogenic Models

2.5.2.1 Spontaneous Models

There is a large variation in lung tumor susceptibility across inbred mouse strains. A/J mice are one of the most sensitive, while BALB/c have intermediate susceptibility with C57BL/6 being almost completely resistant [86]. The natural sensitivity of strains also carries through to chemical induction of lung tumors, such as pure carcinogens or exposure to cigarette smoke as below [86].

Spontaneous lung tumors occurring in susceptible strains of mice have been found to be similar in structure, molecular characteristics and histopathology to human adenocarcinomas [86]. The increase in mouse lung cancer research and confusion over pathologic differences between mouse and human lung cancers has led to new definitions specifically for lung cancer pathology [96].

Through hybrid breeding of the various mouse strains, in particularly A/J with C57BL/6 mice, an inheritance pattern has been observed suggesting that more than one gene is responsible for regulating lung tumor susceptibility [97]. K-Ras expression is believed to be one of the most influential and early-mutated genes causing lung cancer in these models. Other well known genes such as c-MYC, p53, APC, Rb, Mcc, Cdkn2a and Fhit have also been shown to be over expressed or inactivated [86, 98-101].

2.5.2.2 Carcinogenic Models

One of the earliest induction of tumors associated with lung cancer was performed by Angel H. Roffo of Argentina, who induced cancers on the ears of rabbits by rubbing them with tobacco tars, this work helped to shift attention from nicotine to tar as the carcinogenic agent in tobacco smoke [85].

Induction of lung tumors using chemical carcinogens has been a very reproducible and reliable technique with almost identical results in studies performed recently and those performed decades earlier [102]. Potent carcinogens used for induction include polycyclic aromatic hydrocarbons and nitrosamines derived from tobacco and ethyl carbamate (urethane) [91]. The number and size of tumors induced using carcinogens is directly related to the natural susceptibility of different mice strains in spontaneously developing lung cancer as discussed above [91].

Ethyl carbamate, the formal chemical name for Urethane was a routine anesthetic agent used on animals. Once discovered to be the cause of lung adenomas in mice and rats its use as an anesthetic agent diminished [103]. It was later proposed and demonstrated, as shown in Figure 2.25, that vinyl carbamate epoxide, an oxidized off product of ethyle carbamate through two catalyisations by the enzyme cytochrome P450 2E1, was the mutagenic and carcinogenic agent that would then react with DNA. The products of this reaction have miscoding properties and are considered the predominant source of the DNA lesions formed from ethyl carbamate [104-107].

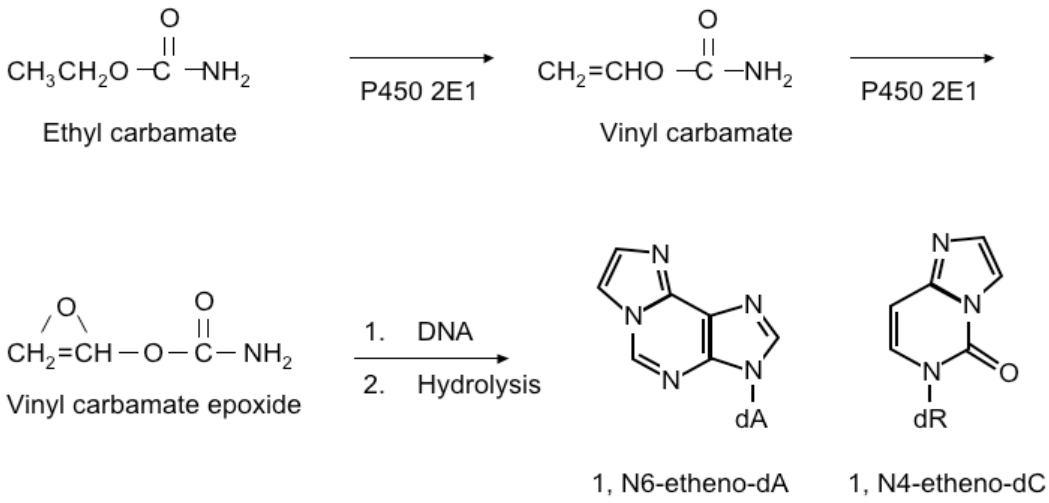

Figure 2.25: Metabolic activation of ethyl carbamate to DNA adducts in the mouse lung, modified from [86].

Two other common carcinogens used for inducing lung tumors include Nitrosamine 4-(methylnitrosamino)-1-(3-pyridyl)-1-butanone (NNK), a tobacco-specific lung

carcinogen, and polycyclic aromatic hydrocarbons (PAHs), a class of environmental carcinogens.

There are many pathways and changes that are still to be discovered in these carcinogen induced mouse lung cancer models. Currently, the formation of specific mutations through reaction with DNA adducts and mutations in critical genes, resulting in lung tumors, has become widely observed and accepted [91].

In this thesis, we focus on the Urethane-induced mouse model of lung cancer for its well-defined induction process and the relatively abundant literature on its carcinogenetic progression. In this model, A/J mice of 6-8 weeks of age are administered with 1mg/g bodyweight of Urethane (Sigma, St Louis) intra peritoneal (IP) [87]. Post carcinogen administration, there is a short period during which a decrease in the number of Clara and alveolar type 2 cells is observed. These cells do recover, and soon surpass the number of cells in normal mice [108]. From these locations, development of adenomas through to adenocarcinomas is thought to occur with some remaining as benign papillary solid adenomas. Malignant adenocarcinomas are rarely shown to metastasize because premature death occurs prior to this transition as the number and size of tumors overburden the respiratory system.

Figure 2.26 represents the timeline of lung tumor carcinogenesis in the Urethane-lung mouse model. Here, we can see the similar cascading pattern of transformation as seen in human lung adenocarcinomas.

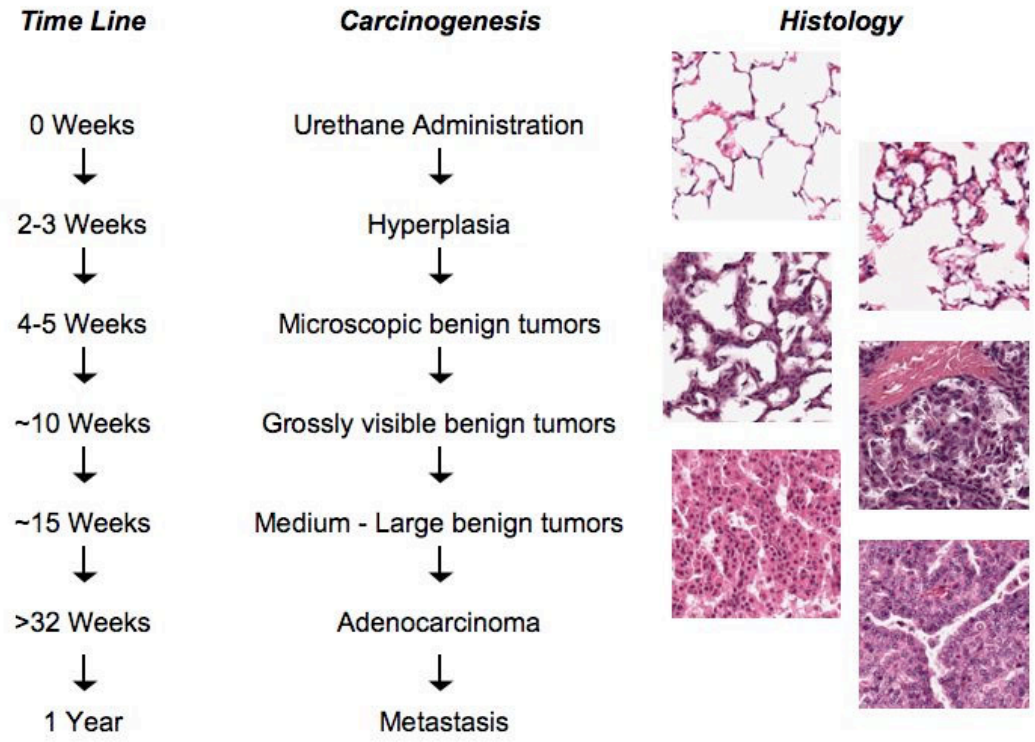

Figure 2.26: Timeline of lung tumor carcinogenesis in the Urethane-induced lung cancer model, recreated from [109].

It is believed that solid tumors are derived from alveolar type II cells. The origins of papillary tumors are still unclear or controversial due to the presence of type II and Clara cell features [110]. One proposal includes a progenitor or self-renewing cancer cell that exhibits the properties of both alveolar type II and Clara cells. Recently, a bronchioalveolar stem cell (BASC) was identified exhibiting properties of alveolar type II and Clara cells. These BASCs have now been targeted as the possible origin for these controversial papillary tumors [111].

While many avenues of research have been investigated there are still many gaps in our understanding of the progression of tumors in this model. The initial genetic, cellular and environmental changes that occur and result in the development of localized hyperplasia in some areas and not in others are still unknown. It is also unknown why some tumors remain benign, while others progress and transform into adenocarcinomas. Finally, the relationship between growth rate and underlying cellular and genetic changes are unclear.

2.5.3 Genetically Manipulated Models

It is widely accepted that normal cells transform into 'cancer' cells through an incremental accumulation of genetic mutations/alterations, resulting in genetic instability. Activation of oncogenes and inactivation of tumor suppressor genes are in essence the mechanisms that trigger oncogenesis. As discussed in Section 2.5.2.1, there are a string of critical gene alterations that have been identified in common lung cancers. These include K-Ras, c-MYC, p53, APC, Rb, Mcc, Cdkn2a and Fhit. These alterations give rise to unregulated cell growth control such as elimination of apoptosis leading to tumor formation.

Activation of mutations in the K-ras have been shown to occur in 25-50% of human lung adenocarcinomas [95]; the conditional activation of the K-ras oncogene is one of the best characterized mouse models of lung cancer[94].

Genetic technologies have enabled a controlled environment for creating models of human disease conditions in the mouse. In particular, novel transgenic and embryonic stem cell knockout techniques have made vast inroads in modeling diseases due to genetic alterations.

2.5.3.1 Transgenic Models

Transgenic techniques are used to manipulate the mouse genome through promotion or ablation of gene function [112]. Using transgenic technology, a gene of interest known as a transgene can be injected into the pronucleus of a single cell embryo that has recently undergone fertilization. This transgene is then incorporated throughout the mouse chromosomes at random locations. The additional DNA is then passed onto all of the differentiating cells of the mouse [113].

Knockout models, in comparison are created through injection of the blastocysts with embryonic stem cells, isolated and modified with a replacement endogenous gene with a homologous DNA segment. This technique does not provide a complete knockout of the gene through out all of the cells, but rather cells are derived from both the implanted embryonic stem cell and the host, resulting in chimeric mice.

In order to study the effects of specific genes in lung tumorigenesis, mouse models have been developed which increase expression of oncogenes [94, 114-116] or decrease expression of tumor-suppressor genes, such as the p53 gene [117], along with single knock out or knock in models [118-120]. Multiple genetic alterations in a single animal have also been developed and shown to increase the aggression of tumor development [121, 122].

Reproducing the complex genetic alterations that occur in human lung cancer will likely require more than an ablation or promotion of a single gene. The limited and lack of spatial and temporal regulation also inhibits many potential alterations that would otherwise be embryonically lethal [119, 123]. Finally, this lack of regulation produces mice that develop multiple types of tumors including lymphomas, liver, kidney and lung adenocarcinomas, increasing the complexity of potential identification of serum markers for lung cancer.

2.5.3.2 Conditional Transgenic Models

Conditional mouse models have recently been introduced to overcome some of the limitations of classical transgenic models discussed above. Here, new techniques are utilized to split the temporal-spatial regulation into individual events [92, 93].

Initial conditional models were based on the principle of gene activator protein-mediated positive regulation of the lac operon in bacteria. Here, a gene of interest is cloned downstream to a regulator sequence that requires at least two molecules to initiate the transcription – a regulator protein and a cognate binding partner [124]. The spatial regulation is obtained through the expression of the regulator protein using a tissue-specific promoter, while the temporal regulation occurs through exogenous supply of the binding partner. An example of such a conditional model is the reverse tetracycline transactivator (rtTA) inducible system. This system has been successfully used to create inducible lung cancer models [125, 126] developing epithelial hyperplasia, adenomatous hyperplasia and finally adenocarcinomas with administration of doxycycline. The same adenocarcinomas have also been shown to regress as the administration of doxycycline was eliminated. This example shows

the potential for conditional systems to reveal the role of a particular gene for tumor maintenance.

Recently, conditional genetic models have been developed to control the site and time at which design-based genetic alterations occur in a strict set of differentiated cells while adjacent cells remain unaltered. These models use a site-specific recombinase to control the enzymatic activity, gene excision, insertion, inversion and translocation [127-129].

A Cre locus of crossover P1 (loxP) recombinase model has been developed to activate K-Ras gene in a mouse model of lung cancer where an adenovirus is used to deliver the Cre activity. Using this model, it has been shown that adenocarcinomas develop in a sporadic manner as seen in human lung NSCLC [130]. This system provides for a robust approach allowing both conditional tumor suppressor genes and oncogenes within the same animal, leading to compound conditional models [121, 131].

The recent strides in genetic engineering have led to the above-discussed mouse modeling techniques. Undoubtedly, many more mouse models will be developed, providing further clues on the genetic changes required for initiation, progression and regression of lung cancer.

2.5.4 Conclusions

Using mouse models techniques, many genetic and molecular events that cause tumorigenesis in the lung have been identified, and many more are still to be discovered. It is unknown which of these events are critical for lung cancer, and a deeper understanding and identification of such events is crucial for the development of early diagnostic and therapeutic strategies. An increasing number of mouse models of lung cancer are now available, continually providing novel approaches for studying these underlying events.

We have chosen the carcinogenic Urethane-induced model since it produces a cascading series of events similar to human lung adenocarcinoma development as

discussed above. This model has also been shown to develop rapidly in its early phases and the ability of the micro-CT to accurately track tumor growth longitudinally will provide greater insight into the growth patterns of this model, both globally and regionally with respect to anatomical structures such as the vascular and pulmonary system.

Many facets of this model are still unknown, including the initial underlying processes that result in the development of localized hyperplasia in some areas and not in others. It is also unknown why some tumors grow at different rates with the majority remaining benign, while some progress and transform into adenocarcinomas.

Is the initial hyperplasia random, and only tumors that are close to major blood supplies continue their pattern of growth? Or is there a regional difference in susceptible mutations? Using the imaging techniques developed in this thesis, such questions can be investigated and regional differences be evaluated.